ChemPubSoc Europe

DOI: 10.1002/chem.201505107

CHEMISTRY A European Journal Full Paper

Metal–Organic Frameworks

Extraordinary Separation of Acetylene-Containing Mixtures with Microporous Metal–Organic Frameworks with Open O Donor Sites and Tunable Robustness through Control of the Helical Chain Secondary Building Units

Zizhu Yao,[a] Zhangjing Zhang,[a] Lizhen Liu,[a] Ziyin Li,[a] Wei Zhou,[b] Yunfeng Zhao,[c, f] Yu Han,[c] Banglin Chen,[d] Rajamani Krishna,*[e] and Shengchang Xiang*[a]

Abstract: Acetylene separation is a very important but challenging industrial separation task. Here, through the solvothermal reaction of CuI and 5-triazole isophthalic acid in different solvents, two metal–organic frameworks (MOFs, **FJU-21** and **FJU-22**) with open O donor sites and controllable robustness have been obtained for acetylene separation. They contain the same paddle-wheel $\{Cu_2(COO)_4\}$ nodes and metal–ligand connection modes, but with different helical chains as secondary building units (SBUs), leading to different structural robustness for the MOFs. **FJU-21** and **FJU-22** are the first examples in which the MOFs' robustness is controlled by adjusting the helical chain SBUs. Good robustness gives the activated **FJU-22a**, which has higher surface area and gas uptakes than the flexible **FJU-21a**. Importantly, FJU-22a shows extraordinary separation of acetylene mixtures under ambient conditions. The separation capacity of **FJU-22a** for 50:50 C_2H_2/CO_2 mixtures is about twice that of the high-capacity HOF-3, and its actual separation selectivity for C_2H_2/C_2H_4 mixtures containing 1% acetylene is the highest among reported porous materials. Based on first-principles calculations, the extraordinary separation performance of C_2H_2 for **FJU-22a** was attributed to hydrogen-bonding interactions between the C_2H_2 molecules with the open O donors on the wall, which provide better recognition ability for C_2H_2 than other functional sites, including open metal sites and amino groups.

Introduction

Removal of acetylene from C_2H_2/C_2H_4 mixtures is an important and highly challenging industrial process.[1–5] Ethylene, the largest volume organic chemical, is widely used for the production of polymers. Ethylene produced in steam crackers typically contains on the order of 1% of acetylene,[6] which should be reduced to an accepted level in the ethylene feed before polymerization, because acetylene can poison Ziegler–Natta catalysts and also lower the resulting product quality.[7] Current approaches to remove acetylene include partial hydrogenation over a noble metal catalyst[8] and the solvent extraction of cracked olefins,[9] but both of these are cost and energy consumptive.

The emerging microporous metal–organic frameworks (MOFs)[10–13] based on physical adsorption are promising as cost-effective and efficient materials for gas separation, which has been a topic of interest because the ability to rationally design and chemically tune their architecture of the MOFs allows chemists to establish various methods to achieve highly selective gas adsorption.[10–29] Since the pioneered work of Kitagawa and co-workers,[14] some MOFs with high acetylene storage have been realized by using immobilized open metal sites (OMS).[30,31] For C_2H_2/C_2H_4 separation, after the first work realized by using the flexible MOFs on the basis of metalloligands in 2011,[2] the series of MOF-74[3] with high densities of open

[a] Z. Yao, Prof. Dr. Z. Zhang, L. Liu, Z. Li, Prof. Dr. S. Xiang
Fujian Provincial Key Laboratory of Polymer Materials
Fujian Normal University, 32 Shangsan Road
Fuzhou 350007 (P. R. China)
E-mail: scxiang@fjnu.edu.cn

[b] Prof. Dr. W. Zhou
NIST Center for Neutron Research, Gaithersburg
Maryland 20899-6102 (USA)

[c] Dr. Y. Zhao, Prof. Dr. Y. Han
Advanced Membranes and Porous Materials Center
Physical Sciences and Engineering Division
King Abdullah University of Science and Technology
Thuwal 23955-6900 (Saudi Arabia)

[d] Prof. Dr. B. Chen
Department of Chemistry, University of Texas at San Antonio
One UTSA Circle, San Antonio, Texas 78249-0698 (USA)

[e] Prof. Dr. R. Krishna
Van't Hoff Institute for Molecular Sciences, University of Amsterdam
Science Park 904
Amsterdam 1098 XH (The Netherlands)

[f] Dr. Y. Zhao
Institute for New Energy Materials & Low-Carbon Technologies
School of Materials Science and Engineering
Tianjin University of Technology, Tianjin 300384 (P. R. China)

Supporting information and ORCID for the author for this article are available on the WWW under http://dx.doi.org/10.1002/chem.201505107.

metal sites and NOTT-300[4] with multiple weak supramolecular interactions were also employed. However, these three kinds of MOFs are not the ideal materials; the former exhibit very low acetylene uptake and the latter two show very low selectivity toward acetylene. A recent MOF, UTSA-100, containing amino groups[5] is a unique example for actual column breakthrough experiments of C_2H_2/C_2H_4 mixtures, giving moderate selectivity and moderate acetylene uptake. Additionally, owing to the similar fluid properties of acetylene and CO_2, the efficient separation of C_2H_2/CO_2 mixture is another technologically interesting issue.[14,28] A few MOFs and zeolites with relevant differences in capacity for C_2H_2/CO_2 have been developed, mainly through tuning the cross-section size of the pore.[32] To date, no MOFs or other porous materials have been found with actual C_2H_2/CO_2 breakthrough experiments, except one hydrogen-bonded organic framework (HOF-3),[33] however, this has low separation capacity. The MOFs for the separation of C_2H_2 mixtures have not been fully explored. It is still desirable to explore new ways to construct the MOFs with excellent performance for the challenging separations of C_2H_2/CO_2 and C_2H_2/C_2H_4 mixtures.

In this work, through solvothermal reactions of 5-triazole isophthalic acid (H_2L), CuI, and various solvents, two MOFs $\{[Cu(L)](DMF)(H_2O)_{1.5}\}_n$ (**FJU-21**, DMF = *N*,*N*′-dimethylformamide) and $\{[Cu(L)]\cdot(DMA)(H_2O)_{1.5}\}_n$ (**FJU-22**, DMA = *N*,*N*′-dimethylacetamide) with open O donor sites and controllable robustness have been obtained for the highly selective separation of both C_2H_2/CO_2 and C_2H_2/C_2H_4 mixtures. This was done on the base of the following considerations. (1) The remarkable difference between C_2H_2 and other gases including CO_2 and ethylene is the acidic hydrogen atoms at both ends of acetylene. Thus, the different framework flexibilities, different OMS and amino groups, and the open O donors can endow the MOFs with exclusive recognition ability for C_2H_2 through extra hydrogen-bonding interactions. (2) The use of 5-triazole isophthalic acid (H_2L) containing one heterocyclic and two carboxylate groups to construct the MOFs may generate rich open O donor sites (without H riding) standing on the framework wall to recognize acetylene. (3) Solvent-induced structure diversity with controllable robustness may be observed to further control the acetylene separation capacity. As expected, the open O donors can provide the MOFs better recognition ability for C_2H_2 than other functional sites, including the OMS and amino groups. The activated **FJU-22a** with open O donors and good robustness exhibits extraordinary separation performances for both C_2H_2/CO_2 and C_2H_2/C_2H_4 mixtures at ambient conditions as demonstrated by gas adsorption, breakthrough simulations, actual column breakthrough experiments, and first-principles calculations.

Results and Discussion

Solvent-induced structure diversity

Green needle-like crystals of **FJU-21** could be obtained in DMF/H_2O (3:2, v/v) mixed solvent at 85 °C for 1 day, and bulk crystals of **FJU-22** could be obtained by the same method

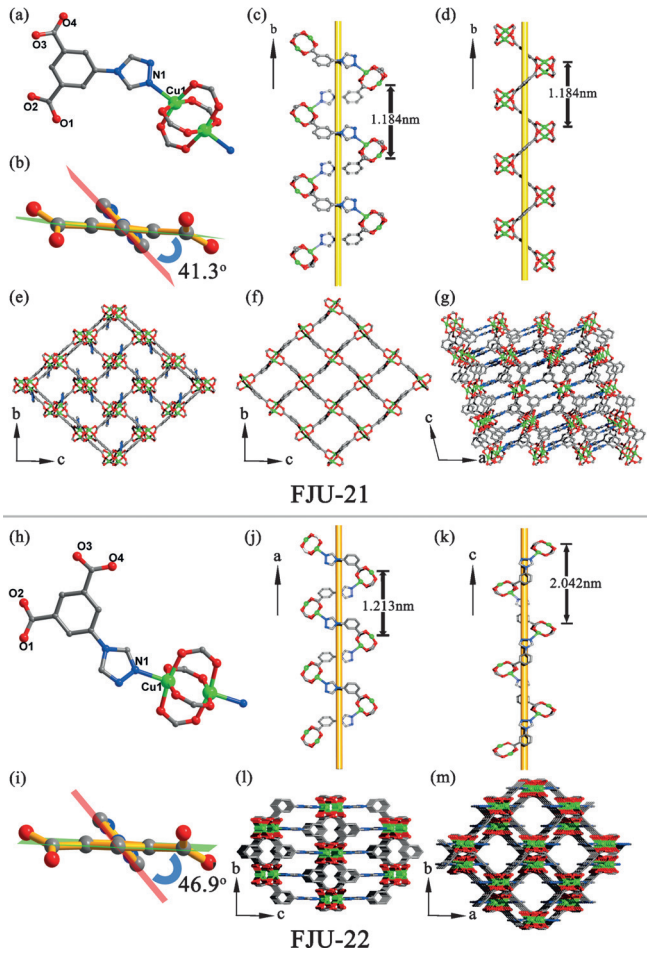

Figure 1. The structures of **FJU-21** (a–g) and **FJU-22** (h–m) showing: the coordination environment of **FJU-21** (a) and **FJU-22** (h); the twist angle between the triazole ring and the plane of the benzene ring of the ligand in **FJU-21** (b) and **FJU-22** (i); the two kinds of helical chain SBUs of **FJU-21** (c and d) along the *b* axis; the unique kind of helical chain SBUs with various pitches along the *a* and *c* axes in **FJU-22** (j and k); the triazole-pillared $[Cu_2(isophthalate)_4]$ bilayers in the orientation of the (200) plane of **FJU-21** (e); the $[Cu_2(isophthalate)_4]$ monolayers in the orientation of the (100) plane of **FJU-21** (f); 3D framework of **FJU-21** along the *b* axis (g); and 3D framework of **FJU-22** view along the *a* and *c* axes (l and m). Color code: Cu, green; C, gray; O, red; N, blue.

except that DMF was replaced by DMA. Single-crystal X-ray diffraction analyses reveal that **FJU-21** and **FJU-22** have the same metal nodes and metal–ligand connection modes (Figure 1). In each crystallographically independent unit, there is one Cu^{II} ion and one ligand. The Cu^{II} ion is fivefold coordinated by four oxygen atoms and one triazolyl N donor from five ligands and has a square-pyramidal coordination environment. Two Cu^{II} ions are bridged by four carboxylate groups to give a paddle-wheel node (PWN). The axial site of the PWN is occupied by triazolyl N donors. The ligand L employs its one triazole N and four carboxylate O atoms to link three PWNs. In **FJU-22**, the twist angle between the triazole ring and the plane of the benzene ring of the ligand L (46.9°) is higher than that of **FJU-21** (41.3°), as shown in Figure 1i and b. The non-planarity of ligand L with various twist angles endows the two MOFs with various helical chains that act as secondary building units

(SBUs). **FJU-22** has a unique type of helical chain SBU with different pitches composed of the PWNs and *N*-benzene triazole linkers along the *a* and *c* axes (Figure 1j and k). The linkage between adjacent SBUs sharing the PWNs results in a three-dimensional (3D) skeleton (Figure 1l and m). **FJU-21** has two types of helical chain SBUs along the *b* axis. One has the same composites as that in **FJU-22** (Figure 1c), which connects with the neighboring SBUs to give triazole-pillared $[Cu_2(isophthalate)_4]$ bilayers in the orientation of the (200) plane (Figure 1e), whereas the other is made up of the PWNs and isophthalate linkers (Figure 1d), and connects with the adjacent SBUs to produce $[Cu_2(isophthalate)_4]$ monolayers oriented at the (100) plane (Figure 1f). The bilayers and monolayers stack on each other by layer-sharing along the *a* axis to form the 3D framework (Figure 1g). By considering the PWN as a six-connected octahedral node and the ligand as a three-connected trigonal linker, the whole frameworks of **FJU-21** and **FJU-22** can be simplified to a (3,6)-connected net with rutile (rtl) and α-PbO_2 (apo) topology, respectively. **FJU-21** shows a 1D channel along the *a* axis (5.00×9.60 Å^2), whereas **FJU-22** also has a 1D channel, but along the *c* axis (7.10×7.10 Å^2; Figure S1 in the Supporting Information). PLATON calculations[34,35] of **FJU-21** and **FJU-22** indicate their void volumes are 923.7 Å^3 (52.1% of the unit cell volume of 1773.3 Å^3) and 1908 Å^3 (52.8% of the unit cell volume of 3614.2 Å^3), respectively.

Owing to the same metal node and metal–ligand connection mode, **FJU-21** and **FJU-22** have similar pore surface structures. Nevertheless, it is worth noting that the solvent-induced structural diversity gives the two MOFs distinct robustness properties. The two as-synthesized MOFs were exchanged with CH_3OH and CH_2Cl_2, respectively, several times, then heated to 60 °C, and evacuated under high vacuum to obtain the desolvated frameworks **FJU-21a** and **FJU-22a.** **FJU-21a** is flexible, whereas **FJU-22a** shows good robustness, as proved by powder X-ray diffraction experiments (PXRD; Figure S2 in the Supporting Information). For **FJU-22**, with the one unique type of helical chain SBU, the 2θ values are not shifted for the activated sample compared to the as-synthesized sample pattern. However, for **FJU-21**, which contains one more type of helical chain SBU, the values of 2θ for the (100) and (002) planes are shifted to higher angles for the activated sample, and no shift for the (020) plane is seen, indicating that the dynamic features are down to the $[Cu_2(isophthalate)_4]$ monolayers oriented at the (100) plane and constructed from the helical chains exclusively in **FJU-21** and not observed in **FJU-22**. In addition, if exposed to air or water vapor, the values of 2θ for **FJU-21** are shifted, whereas for **FJU-22** there is no obvious change under the same conditions, further indicating that **FJU-22** has better stability than **FJU-21**. Although several methods including those using high-valent metal ions,[36] modulated synthesis,[37] N-donor ligands,[38] and superhydrophobic ligands[39] have been proposed to enhance MOF stability, **FJU-21** and **FJU-22** are the first examples to demonstrate control of MOF stability and robustness by adjusting the helical chain SBUs.

Gas adsorption

To assess the permanent porosity, the N_2 sorption isotherms of the activated **FJU-21a** and **FJU-22a** materials were examined at 77 K (Figure 2), which yielded a reversible type I isotherm for the microporous nature of the samples with Brunauer–Emmett–Teller (BET) surface areas of 369.10 and 828.19 m^2g^{-1}, respectively. **FJU-21a** shows a bimodal pore size distribution centered at 5.2 and 8.7 Å, and **FJU-22a** has a distribution centered at 8.0 Å, as calculated by the non-local (NL)-DFT method; these values are close to the pore sizes determined from the crystal structures (Figure S1 in the Supporting Information). Although their void volumes from the Platon calculations are close, the BET surface area for **FJU-21a**, with the dynamic framework, is only about half that for **FJU-22a**. The flexible character of **FJU-21** is further confirmed by a hysteresis loop in the N_2 adsorption isotherm at 77 K.

The unique pore structures encouraged us to examine the capacities of the two MOFs for gas adsorption. The low-pressure sorption isotherms of CO_2, C_2H_2, and C_2H_4 were collected at 273 and 296 K (Figure 2 and Figure S3 in the Supporting Information). At 296 K and 1 bar, **FJU-22a** can adsorb 111.3, 114.8, and 85.8 cm^3g^{-1} of CO_2, C_2H_2, and C_2H_4, respectively. The adsorption isotherms for C_2H_2, CO_2, and C_2H_4 on **FJU-21a** are very similar to those for **FJU-22a** and the adsorption capacity follows the same hierarchy: $C_2H_2 > CO_2 > C_2H_4$. This phenomenon may be attributed to the same pore surface structure resulting from the same metal node and ligand connection mode. However, the halved BET surface area for **FJU-21a** makes its various gas uptakes fall to half the corresponding values of **FJU-22a**. Furthermore, it is worth noting that the acetylene uptake isotherms for **FJU-21a** and **FJU-22a** at 296 K show a very sharp uptake at low pressure, whereas carbon dioxide uptake is much lower at this pressure. This discovery motivated us to examine their feasibility for the industrially important C_2H_2/CO_2 separation.

C_2H_2/CO_2 column breakthrough experiments

We first performed breakthrough simulations for a 50:50 (v/v) C_2H_2/CO_2 mixture on **FJU-21a** and **FJU-22a** by using the established methodology.[40] As shown in Figure S4 (in the Supporting Information), **FJU-21a** and **FJU-22a** are able to separate C_2H_2 from the C_2H_2/CO_2 mixture at room temperature. Clearly, **FJU-22a**, with good robustness, is more effective than **FJU-21a** for the C_2H_2/CO_2 separation. Thus, we only studied the actual performance of **FJU-22a** in the experimental column breakthrough.

In the actual column breakthrough experiment, an equimolar C_2H_2/CO_2 mixture was flowed over a packed column of the **FJU-22a** solid with a total flow of 5 $cm^3\,min^{-1}$ at 296 K (Figure 3). CO_2 was detected after the gas mixture has been introduced into the column for about 12 min, whereas C_2H_2 was not detected until a breakthrough time of 23 min was reached. Thus, the separation of C_2H_2/CO_2 mixture gases through a column packed with **FJU-22a** solid can be achieved efficiently. The breakthrough times of CO_2 and C_2H_2 on the unique

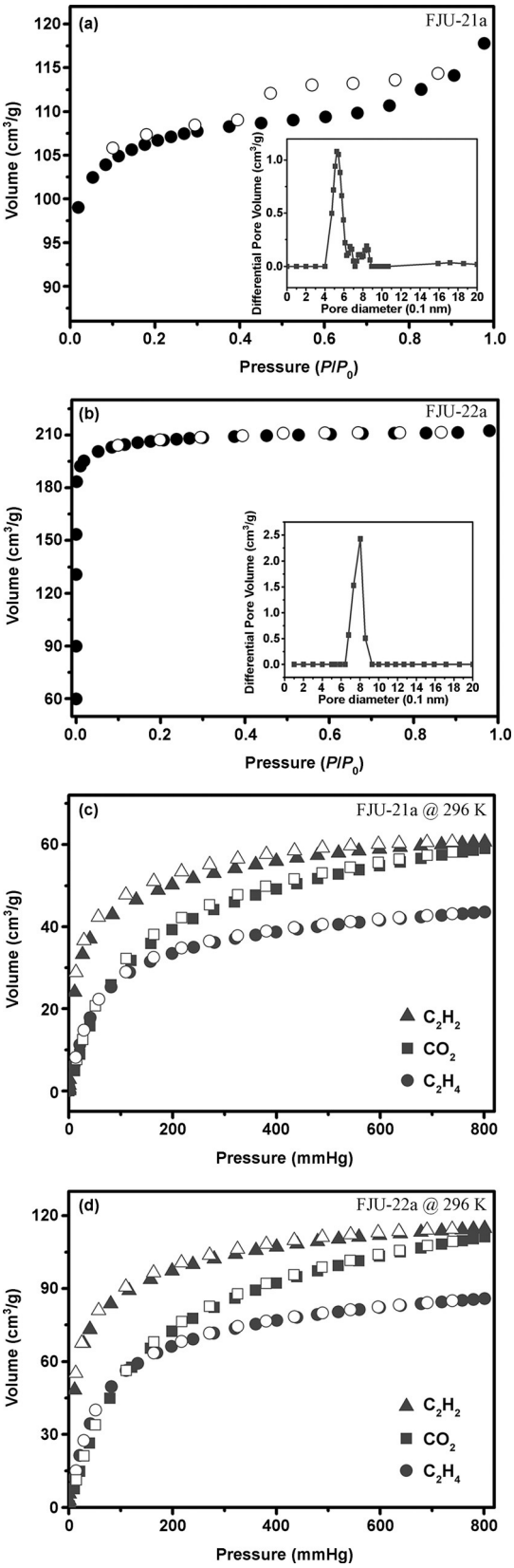

Figure 2. N_2 sorption isotherm and pore-size distributions at 77 K of **FJU-21a** (a) and **FJU-22a** (b). Adsorption isotherms for C_2H_2, CO_2, and C_2H_4 on **FJU-21a** (c) and **FJU-22a** (d) at 296 K (solid symbols: adsorption; open symbols: desorption).

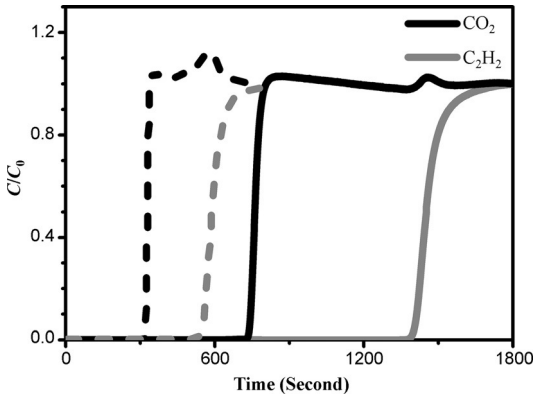

Figure 3. Experimental column breakthrough curve for an equimolar C_2H_2/CO_2 mixture in an adsorber bed packed with **FJU-22a** (——) or HOF-3a (-----) at ambient conditions (296 K, 1 bar). The total flow is of 5 $cm^3 min^{-1}$.

pore material HOF-3 were 5.5 and 9 min, respectively.[33] From the breakthrough curve, the separation selectivity, $\alpha = (q_1 y_2)/(y_1 q_2)$, for **FJU-22a** is 1.9, and close to 2.0 for HOF-3. However, **FJU-22a** has a separation capacity of 44.13 $cm^3 g^{-1}$, which is much higher than the value of 25.54 $cm^3 g^{-1}$ for HOF-3. At the same separation conditions, **FJU-22a**, with the open O donors, shows better performance than HOF-3, containing functional amino groups. **FJU-22a** is the first example of a MOF whose separation of a C_2H_2/CO_2 mixture has been clearly established by column breakthrough experiments.

First-principles calculations

To further understand the C_2H_2 and CO_2 adsorption on **FJU-22a**, detailed computational investigations were performed. We first optimized the bare **FJU-22a** structure by first-principles DFT-D (dispersion-corrected density-functional theory) calculations,[41] and then carried out Grand Canonical Monte Carlo (GCMC) simulations by using the classical force-field method. Based on the probability distribution of adsorbed gas molecules generated from the GCMC simulations, we introduced C_2H_2/CO_2 accordingly into the **FJU-22a** channel pore, and further optimized the structures by using DFT-D. We found that the guest molecules are associated with particular adsorption sites. Upon adsorption, both C_2H_2 and CO_2 sit right at the small cage connecting the two adjacent channel pores (Figure 4 and Figure S5 in the Supporting Information). Although the linker triazole ring has van der Waals (vdW) interactions with C_2H_2, the relatively strong binding between C_2H_2 and **FJU-22a** clearly comes from the hydrogen-bonding interactions between the C_2H_2 and the framework O ($d[O(\text{-}CO_2)\cdots H(C_2H_2)] = 2.290$ Å); this interaction does not exist between CO_2 and **FJU-22a** and CO_2 adsorption in the structure is mainly vdW-type in nature. The static C_2H_2 and CO_2 binding energies for **FJU-22a**, derived from the DFT-D calculations, are 33.3 and 22.6 kJ mol^{-1}, respectively. This difference in the gas/MOF framework interaction strength is likely the reason why the performance of separation for C_2H_2/CO_2 is outstanding in **FJU-22a** at room temperature.

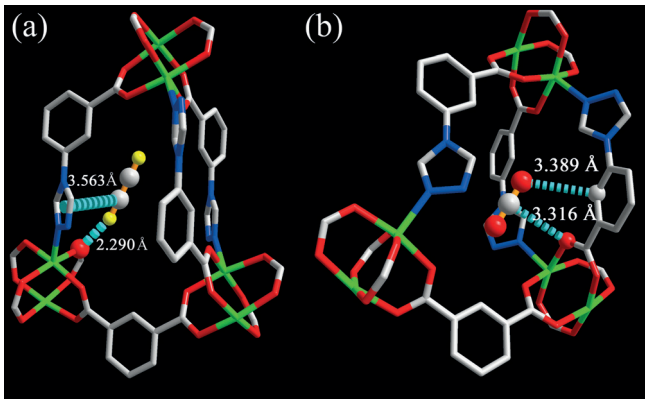

Figure 4. The C_2H_2 (a) and CO_2 (b) molecules sit right at the small cage connecting the two adjacent channel pores. Multiple-point interactions of the C_2H_2 with framework: d[O(-CO_2)···H(C_2H_2)] = 2.290 Å, d[center(-triazolyl)-···C(C_2H_2)] = 3.563 Å; multiple-point interactions between CO_2 molecule and the framework: d[O(-CO_2)···C(CO_2)] = 3.316 Å, d[C(-benzene)-···O(CO_2)] = 3.389 Å. Color code: Cu, green; C, gray; H, yellow; O, red; N, blue.

C_2H_2/C_2H_4 breakthrough experiments

The performance of **FJU-22a** for the removal of acetylene from C_2H_2/C_2H_4 mixtures containing 1% acetylene was examined through experimental column breakthrough in which a C_2H_2/C_2H_4 (1:99, v/v) mixture was flowed over a packed column of the **FJU-22a** solid with a total flow of 1.8 $cm^3 min^{-1}$ at 296 K. As shown in Figure 5, the separation of the C_2H_2/C_2H_4

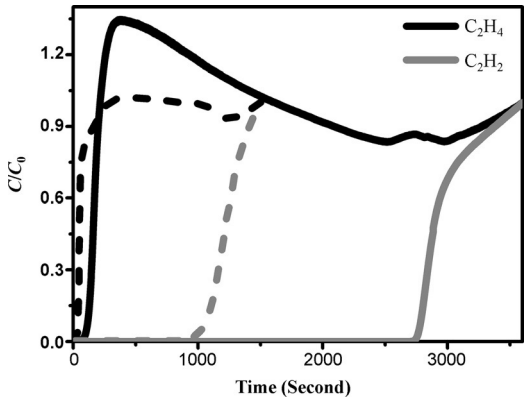

Figure 5. Experimental column breakthrough curve for an C_2H_2/C_2H_4 (1:99, v/v) mixture in an adsorber bed packed with **FJU-22a** (——) and UTSA-100a (-----) at ambient conditions (296 K, 1 bar). The total flows are 1.8 $cm^3 min^{-1}$ for **FJU-22**a and 2 $cm^3 min^{-1}$ for UTSA-100a.

mixture gases through a column packed with **FJU-22a** solid can be efficiently achieved, and the separation selectivity, α, for C_2H_2/C_2H_4 is 25.8. The adsorption and separation data for C_2H_2 and C_2H_4 gases on **FJU-22a** and some representative MOFs are given in Figure 6 and Table S4 (in the Supporting Information). M'MOF-3a, with a flexible framework, exhibits relative high separation selectivity (24.0), but very low acetylene uptakes, because of narrow pores and high sieving effects.[2] High densities of open metal sites can significantly endow the

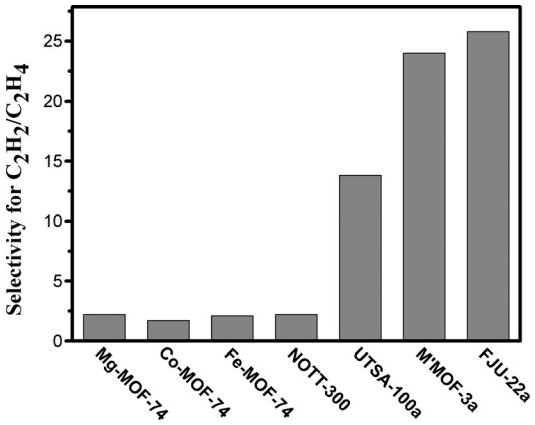

Figure 6. Selectivity for C_2H_2/C_2H_4 mixtures of some representative MOFs.

series of MOF-74 with high acetylene uptakes, but their selectivities for C_2H_2/C_2H_4 separation are systemically quite low[3] as the open metal sites have quite strong interactions toward both ethylene and acetylene molecules. NOTT-300 has multiple weak supramolecular interactions aligned within the host to form an optimal geometry for the selective binding of hydrocarbons, but the selectivity toward C_2H_2/C_2H_4 is still very low.[4] The multiple supramolecular interactions in NOTT-300 include the hydrogen-bonding interactions between C(C_2H_2 or C_2H_4) and H-O(framework), which are clearly distinct from those between O(framework) and H-C(C_2H_2) in **FJU-22a**. The former cannot recognize acetylene and ethylene very well, whereas the latter endows **FJU-22a** with exceptionally high selectivity. UTSA-100a,[5] containing amino groups with dual functionalities to simultaneously bind acetylene and sieve ethylene, has a relative high selectivity, about five times that for MOFs containing OMS. It is worth noting that **FJU-22** is isostructural with UTSA-100. The enthalpies of acetylene adsorption on both MOFs are almost same, but the separation selectivity, α, of **FJU-22a** is more than twice that for UTSA-100a, indicating that even in UTSA-100a (Figure S6 in the Supporting Information), the main contribution for its high selectivity toward acetylene may also come from the open O donor sites on the framework wall, rather than the amino groups. Conversely, the extra amino groups of UTSA-100a, to a certain extent, decrease its static C_2H_2 uptake. Despite its moderate static acetylene uptake, **FJU-22a** has the highest separation selectivity for the C_2H_2/C_2H_4 mixture among the reported porous materials. Based on the discussion above, open O donors on the pore wall can provide MOFs with better recognition for C_2H_2/C_2H_4 mixtures than the OMS and amino groups. **FJU-22a** is thus superior to the other MOFs, exhibiting highly efficient removal of acetylene from ethylene/acetylene mixtures containing 1% acetylene.

Conclusions

We have observed solvent-induced topological diversity enabling controllable robustness in two metal–organic frameworks (**FJU-21** and **FJU-22**) and have demonstrated that microporous

MOFs with open O sites are highly selective for the separation of C_2H_2/CO_2 and C_2H_2/C_2H_4 at ambient conditions. Control of the MOFs' robustness through tuning the helical chain SBUs is shown to be an efficient design approach for the first time. The good robustness of the activated **FJU-22a**, with open O donors, results in the extraordinary separation performance for mixtures of C_2H_2/CO_2 and C_2H_2/C_2H_4; this performance is superior to all the reported MOFs including the flexible **FJU-21a**. The separation capacity of **FJU-22a** for 50:50 C_2H_2/CO_2 mixtures is about twice that of HOF-3, the unique example for separation before our experiments. The actual selectivity of **FJU-22a** for C_2H_2/C_2H_4 mixtures containing 1% C_2H_2 is highest among the reported porous materials. Such preferential adsorption for C_2H_2 by **FJU-22a** rather than CO_2 and C_2H_4 is attributed to the open O donor sites on its framework wall. Open O donors can provide MOFs with better recognition ability for C_2H_2 than other functional sites, including open metal sites (OMS) and amino groups. It is expected that extensive research endeavors on porous MOFs will facilitate the discoveries of better C_2H_2 separation materials.

Experimental Section

General

All reagents and solvents were used as received from commercial suppliers without further purification. Thermogravimetric analyses (TGA) were performed with a Mettler Toledo TGA/SDTA851^e analyzer with a nitrogen flow and a heating rate of 10 K min^{-1} from 30 °C to 600 °C. Elemental analysis was collected with a Vario EL III elemental analyzer to give a ratio of C/H/N. Powder X-ray diffraction (PXRD) was carried out with a PANalytical X'Pert^3 powder diffractometer equipped with a Cu sealed tube ($\lambda = 1.54178$ Å) at 40 kV and 40 mA over the 2θ range 5–25°.

Synthesis

***N*,*N*-Dimethylformamide azine dihydrochloride (DMAz)**: The DMAz used in this study was synthesized by a modified version of the method in refs. [42,43]. Thionyl chloride ($SOCl_2$, 28.6 mL, 0.4 mol) was added with stirring to DMF (150 mL) at 5 °C. After addition, this mixture was kept at 5 °C for 24 h and then aqueous hydrazine hydrate (5 mL, 0.1 mol) in DMF (20 mL) was added slowly. After addition, the mixture was stirred at room temperature for 48 h and the white precipitate of *N*,*N*-dimethylformamide azine dihydrochloride was collected by filtration and washed with DMF and diethyl ether. Yield: 19.1 g; m.p.: 251 °C.

5-Triazole isophthalic acid (H_2L): A mixture of *N*,*N*-dimethylformamide azine dihydrochloride (4.0 g, 18.66 mmol) and 5-amino isophthalic acid (3.38 g, 18.66 mmol) was heated at reflux in 1,2-dimethylbenzene (50 mL) for 16 h to obtain a white solid. The solid was filtered and washed with ethanol (2×15 mL) and diethyl ether (1×17 mL). Yield: 1.62 g, 37.3%.

$\{[Cu(L)](DMF)(H_2O)_{1.5}\}_n$ (FJU-21): A mixture of CuI (0.1 mmol, 0.0191 g), H_2L (0.1 mmol, 0.0223 g), DMF (3 mL), and H_2O (2 mL) was stirred for 10 min. Then, the solution was transferred to a 23 mL glass reactor and heated to 85 °C. After 24 h, the system was cooled to room temperature and green needle-like crystals were obtained (32% yield with regard to H_2L). Elemental analysis calcd (%) for **FJU-21**: C 39.49, H 3.80, N 14.18; found: C 40.23, H 3.87, N 14.42.

$\{[Cu(L)]\cdot(DMA)(H_2O)_{1.5}\}_n$ (FJU-22): **FJU-22** was obtained by the same procedure used for preparation of **FJU-21** except that the DMF was replaced with DMA. Green bulk crystals of **FJU-22** were obtained (37% yield with regard to H_2L). Elemental analysis calcd (%) for **FJU-22**: C 41.08, H 4.16, N 13.69; found: C 41.78, H 4.21, N 14.05.

Single-crystal X-ray structure determination

Data collection and structural analysis of the crystals were collected on an Agilent Technologies SuperNova Single Crystal Diffractometer equipped with graphite monochromatic Cu K_α radiation ($\lambda = 1.54184$ Å). The crystal was kept at 293(10) K during data collection. Using Olex2,[44] the structure was solved with the Superflip structure solution program by using charge flipping and refined with the ShelXL refinement package by using least-squares minimization. The hydrogen atoms on the ligands were placed in idealized positions and refined by using a riding model. We employed PLATON[34]/SQUEEZE[35] to calculate the diffraction contribution of the solvent molecules in **FJU-21** and **FJU-22** and thereby produce a set of solvent-free diffraction intensities. The formulae of the crystals were calculated by elemental analysis. The detailed crystallographic data and structure refinement parameters for these compounds are summarized in the Supporting Information, Table S1. CCDC 1421052 (**FJU-21**) and 1421054 (**FJU-22**) contain the supplementary crystallographic data for this paper. These data are provided free of charge by The Cambridge Crystallographic Data Centre.

Gas adsorption measurements

A Micromeritics ASAP 2020 surface area analyzer was used to measure the gas adsorption. The sorption measurements were performed at 77 K with liquid nitrogen and at 273 K with an ice/water bath (slush). A water bath was used for adsorption isotherms at 296 K. DFT pore size distributions and pore sizes were calculated from the N_2 adsorption at 77 K.

Transient breakthrough simulations

The performance of industrial fixed-bed adsorbers is dictated by a combination of adsorption selectivity and uptake capacity. For a proper comparison of various MOFs, we performed transient breakthrough simulations by using the simulation methodology.[40] For the breakthrough simulations, the following parameter values were used: length of packed bed, $L = 0.3$ m; voidage of packed bed = 0.4; superficial gas velocity at inlet, $u = 0.04$ m s^{-1}. The framework density of **FJU-21** is 1104 kg m^{-3} and for **FJU-22** it is 1083 kg m^{-3}.

Column breakthrough test set-up, procedures, and measurements

The mixed-gas breakthrough separation experiment was conducted at 296 K by using a laboratory-scale fix-bed reactor. In a typical breakthrough experiment (Figure S7 in the Supporting Information) for the C_2H_2/CO_2 mixture, **FJU-22** powder (1.2 g) was packed into a quartz column (5.8 mm I.D.×150 mm) with silica wool filling the void space. The sorbent was activated in situ in the column with a vacuum pump at 333 K for 24 h. A helium flow (5 cm^3 min^{-1}) was introduced after the activation process to purge the adsorbent. The flow of He was then turned off while a gas mixture of C_2H_2/CO_2 (50:50, v/v) at 5 cm^3 min^{-1} was allowed to flow into the column. The effluent from the column was monitored by

using a mass spectrometer (MS). The absolute adsorbed amount of gas i (q_i) is calculated from the breakthrough curve by Equation (1):

$$q_i = \frac{F_i x t_0 - V_{dead} - \int_0^{t_0} F_e \Delta t}{m} \quad (1)$$

in which F_i is the influent flow rate of the specific gas ($cm^3 min^{-1}$), t_0 is the adsorption time (min), V_{dead} is the dead volume of the system (cm^3), F_e is the effluent flow rate of the specific gas ($cm^3 min^{-1}$), and m is the mass of the sorbent (g). The separation factor (α) of the breakthrough experiment is determined as:

$$\alpha = \frac{q_1 y_2}{y_1 q_2} \quad (2)$$

in which y_i is the molar fraction of gas i in the gas mixture. The column breakthrough measurement for C_2H_2/C_2H_4 (1:99, v/v) mixtures was similar to the measurements for the C_2H_2/CO_2 mixture, except that the helium flow was changed to 1.8 $cm^3 min^{-1}$.

Details of DFT-D calculations and GCMC simulations

First-principles calculations based on density-functional theory were performed by using the PWSCF package.[41] A semiempirical addition of dispersive forces to conventional DFT[45] was included in the calculation to account for van der Waals interactions. We used Vanderbilt-type ultrasoft pseudopotentials and the generalized gradient approximation (GGA) with the Perdew–Burke–Ernzerhof (PBE) exchange correlation. A cutoff energy of 544 eV and a $2\times2\times2$ k sampling were sufficient for the total energy to converge within 0.5 meV per atom. We first optimized the bare **FJU-22** structure. The optimized structure is fairly close to the experimental structure determined from XRD. C_2H_2 or CO_2 molecules were then introduced to the optimized HOF structure (guided by the GCMC result), followed by a full structural relaxation. To obtain the gas binding energies, a free gas molecule placed in a supercell with the same cell dimensions was also relaxed as a reference. The static binding energy was then calculated by using: $E_B = [E(MOF) + nE(gas) - E(MOF + ngas)]/n$. Grand Canonical Monte Carlo (GCMC) simulations[46] were performed for C_2H_2/CO_2 adsorption on **FJU-22**, with the gas molecules and the MOF frameworks both treated as rigid bodies. A $2\times2\times2$ supercell was used as the simulation box to ensure the simulation accuracy. A total of 2×10^7 steps were used for equilibration and an additional 2×10^7 steps were used to calculate the ensemble average of gas adsorption sites and thermodynamic properties. We used the standard universal force field (UFF)[47] to describe the gas–framework interaction and the gas–gas interaction. Atomic partial charges derived from first-principles calculations were included in the simulation to account for electrostatic interactions. The cut-off radius used for the Lennard–Jones interactions is 12.8 Å. The long-range electrostatic interactions were treated by using the Ewald summation technique with tin-foil boundary condition. Simulations were performed at various temperatures and pressures. The probability distributions of adsorbed C_2H_2 and CO_2 were generated from the simulation after the equilibrium stage.

Acknowledgments

This work was financially supported by the National Natural Science Foundation of China (21207018, 21273033, 21203024, and 21573042) and the Fujian Science and Technology Department (2014J06003 and 2014H6007). S.X. gratefully acknowledges the support of the Recruitment Program of Global Young Experts, Program for New Century Excellent Talents in University (NCET-10-0108), and the Award 'MinJiang Scholar Program' in Fujian Province.

Keywords: column breakthrough · metal–organic frameworks · open O donors · selective gas adsorption · structural diversity

[1] F. Studt, F. Abild-Pedersen, T. Bligaard, R. Z. Sørensen, C. H. Christensen, J. K. Nøskov, *Science* **2008**, *320*, 1320–1322.
[2] S. C. Xiang, Z. J. Zhang, C. G. Zhao, K. L. Hong, X. B. Zhao, D. R. Ding, M. H. Xia, C. D. Wu, M. C. Das, R. Gill, K. M. Tomoas, B. L. Chen, *Nat. Commun.* **2011**, *2*, 204.
[3] a) E. D. Bloch, W. L. Queen, R. Krishna, J. M. Zadrozny, C. M. Brown, J. R. Long, *Science* **2012**, *335*, 1606–1610; b) Y. B. He, R. Krishna, B. L. Chen, *Energy Environ. Sci.* **2012**, *5*, 9107–9120.
[4] S. H. Yang, A. J. Ramirez-Cuesta, R. Newby, V. Garcia-Sakai, P. Manuel, S. K. Callear, S. I. Campbell, C. C. Tang, M. Schröder, *Nat. Chem.* **2014**, *7*, 121–129.
[5] T. L. Hu, H. L. Wang, B. Li, R. Krishna, H. Wu, W. Zhou, Y. F. Zhao, Y. Han, X. Wang, W. D. Zhu, Z. Z. Yao, S. C. Xiang, B. L. Chen, *Nat. Commun.* **2015**, *6*, 7328.
[6] B. M. Collins, US Patent 4126645, **1978**.
[7] W. Huang, J. R. McCormick, R. F. Lobo, J. G. Chen, *J. Catal.* **2007**, *246*, 40–51.
[8] a) B. M. Choudary, M. Lakshmi Kantam, N. Mahender Reddy, K. Koteswara Rao, Y. Haritha, V. Bhaskar, F. Figueras, A. Tuel, *Appl. Catal. A* **1999**, *181*, 139–144; b) N. A. Khan, S. Shaikhutdinov, H. J. Freund, *Catal. Lett.* **2006**, *108*, 159–164.
[9] K. Weissermel, H. J. Arpe, *Industrial Organic Chemistry*, 4th ed., 91–98, Wiley-VCH, Weinheim, **2003**.
[10] a) H. Furukawa, K. E. Cordova, M. O'Keeffe, O. M. Yaghi, *Science* **2013**, *341*, 1230444; b) J. R. Long, O. M. Yaghi, *Chem. Soc. Rev.* **2009**, *38*, 1213–1214.
[11] a) H. C. Zhou, S. Kitagawa, *Chem. Soc. Rev.* **2014**, *43*, 5415–5418; b) H. Sato, W. Kosaka, R. Matsuda, A. Hori, Y. Hijikata, R. V. Belosludov, S. Sakaki, M. Takata, S. Kitagawa, *Science* **2014**, *343*, 167–170.
[12] G. Férey, C. Serre, *Chem. Soc. Rev.* **2009**, *38*, 1380–1399.
[13] a) S. J. Bao, R. Krishna, Y. B. He, J. S. Qin, Z. M. Su, S. L. Li, W. Xie, D. Y. Du, W. W. He, S. R. Zhang, Y. Q. Lan, *J. Mater. Chem. A* **2015**, *3*, 7361–7367; b) S. L. Li, Y. Q. Lan, H. Sakurai, Q. Xu, *Chem. Eur. J.* **2012**, *18*, 16302–16309; c) Q. L. Zhu, Q. Xu, *Chem. Soc. Rev.* **2014**, *43*, 5468–5512; d) J. K. Sun, Q. Xu, *Energy Environ. Sci.* **2014**, *7*, 2071–2100; e) J. S. Li, Y. J. Tang, S. L. Li, S. R. Zhang, Z. H. Dai, Z. H. Si, Y. Q. Lan, *CrystEngComm* **2015**, *17*, 1080–1085; f) D. Y. Du, J. S. Qin, S. L. Li, Z. M. Su, Y. Q. Lan, *Chem. Soc. Rev.* **2014**, *43*, 4615–4632.
[14] R. Matsuda, R. Kitaura, S. Kitagawa, Y. Kubota, R. V. Belosludov, T. C. Kobayashi, H. Sakamoto, T. M. Takata, Y. Kawazoe, T. Chiba, Y. Mita, *Nature* **2005**, *436*, 238–241.
[15] a) J. B. Lin, W. Xue, J. P. Zhang, X. M. Chen, *Chem. Commun.* **2011**, *47*, 926–928; b) P. Q. Liao, H. Y. Chen, D. D. Zhou, S. Y. Liu, C. T. He, Z. B. Rui, H. B. Ji, J. P. Zhang, X. M. Chen, *Energy Environ. Sci.* **2015**, *8*, 1011–1016.
[16] a) A. Samanta, A. Zhao, G. K. H. Shimizu, P. Sarkar, R. Gupta, *Ind. Eng. Chem. Res.* **2012**, *51*, 1438–1463; b) R. Vaidhyanathan, S. S. Iremonger, G. K. H. Shimizu, P. G. Boyd, S. Alavi, T. K. Woo, *Angew. Chem. Int. Ed.* **2012**, *51*, 1826–1829; *Angew. Chem.* **2012**, *124*, 1862–1865; c) R. Vaidhyanathan, S. S. Iremonger, K. W. Dawsona, G. K. H. Shimizu, *Chem. Commun.* **2009**, 5230–5232.

[17] a) X. Zhao, X. H. Bu, Q. G. Zhai, H. Tran, P. Y. Feng, *J. Am. Chem. Soc.* **2015**, *137*, 1396 – 1399; b) Q. G. Zhai, Q. Lin, T. Wu, L. Wang, S. T. Zheng, X. H. Bu, P. Y. Feng, *Chem. Mater.* **2012**, *24*, 2624 – 2626; c) Q. Lin, T. Wu, S. T. Zheng, X. H. Bu, P. Y. Feng, *J. Am. Chem. Soc.* **2012**, *134*, 784 – 787.

[18] a) J. G. Duan, W. Q. Jin, R. Krishna, *Inorg. Chem.* **2015**, *54*, 4279 – 4284; b) Y. P. Chen, Y. Y. Liu, D. H. Liu, M. Bosch, H. C. Zhou, *J. Am. Chem. Soc.* **2015**, *137*, 2919 – 2930; c) C. Wang, D. M. Liu, W. B. Lin, *J. Am. Chem. Soc.* **2013**, *135*, 13222 – 13234; d) W. J. Wang, D. Q. Yuan, *Sci. Rep.* **2014**, *4*, 5711.

[19] a) J. Y. Lee, L. Pan, X. Y. Huang, T. J. Emge, J. Li, *Adv. Funct. Mater.* **2011**, *21*, 993 – 998; b) H. Liu, Y. G. Zhao, Z. J. Zhang, N. Nijem, Y. J. Chabal, H. P. Zeng, J. Li, *Adv. Funct. Mater.* **2011**, *21*, 4754 – 4762; c) Y. Chen, H. Wang, J. Li, J. V. Lockard, *J. Mater. Chem. A J. Mater. Chem. A.* **2015**, *3*, 4945 – 4953; d) H. Wang, K. Yao, Z. Zhang, J. Jagiello, Q. Gong, Y. Han, J. Li, *Chem. Sci.* **2014**, *5*, 620 – 624.

[20] a) X. Duan, J. F. Cai, J. C. Yu, C. D. Wu, Y. J. Cui, Y. Yang, G. D. Qian, *Microporous Mesoporous Mater.* **2013**, *181*, 99 – 104; b) T. F. Xia, J. F. Cai, H. Z. Wang, X. Duan, Y. J. Cui, Y. Yang, G. D. Qian, *Microporous Mesoporous Mater.* **2015**, *215*, 109 – 115.

[21] M. Fischer, F. Hoffmann, M. Froeba, *ChemPhysChem* **2010**, *11*, 2220 – 2229.

[22] J. W. Yoon, J. S. Lee, S. Lee, K. H. Cho, Y. K. Hwang, M. Daturi, C. H. Jun, R. Krishna, J. S. Chang, *Chem. Eur. J* **2015**, *50*, 18431 – 18438.

[23] H. M. Wen, B. Li, H. L. Wang, R. Krishna, B. L. Chen, *Chem. Commun.* **2016**, *52*, 1166 – 1169.

[24] Y. B. He, S. C. Xiang, B. L. Chen, *J. Am. Chem. Soc.* **2011**, *133*, 14570 – 14573.

[25] M. C. Das, Q. S. Guo, Y. B. He, J. Kim, C. G. Zhao, K. Hong, S. C. Xiang, Z. J. Zhang, K. M. Thomas, R. Krishna, B. L. Chen, *J. Am. Chem. Soc.* **2012**, *134*, 8703 – 8710.

[26] S. J. Lee, J. W. Yoon, Y. K. Seo, M. B. Kim, S. K. Lee, U. H. Lee, Y. K. Hwang, Y. S. Bae, J. S. Chang, *Microporous Mesoporous Mater.* **2014**, *193*, 160 – 165.

[27] H. M. Wen, B. Li, H. L. Wang, C. Wu, K. Alfooty, R. Krishnad, B. L. Chen, *Chem. Commun.* **2015**, *51*, 5610 – 5613.

[28] Z. J. Zhang, S. C. Xiang, B. L. Chen, *CrystEngComm* **2011**, *13*, 5983 – 5992.

[29] a) Z. J. Zhang, Z. Z. Yao, S. C. Xiang, B. L. Chen, *Energy Environ. Sci.* **2014**, *7*, 2868 – 2899; <lit b>S. C. Xiang, Y. B. He, Z. J. Zhang, H. Wu, W. Zhou, R. Krishna, B. L. Chen, *Nat. Commun.* **2012**, *3*, 954.

[30] a) S. C. Xiang, W. Zhou, Z. J. Zhang, M. A. Green, Y. Liu, B. L. Chen, *Angew. Chem. Int. Ed.* **2010**, *49*, 4615 – 4618; *Angew. Chem.* **2010**, *122*, 4719 – 4722; b) S. C. Xiang, W. Zhou, J. M. Gallegos, Y. Liu, B. L. Chen, *J. Am. Chem. Soc.* **2009**, *131*, 12415 – 12419; c) C. L. Song, J. Y. Hu, Y. J. Ling, Y. L. Feng, D. L. Chen, Y. B. He, *Dalton Trans.* **2015**, *44*, 14823 – 14829.

[31] J. D. Pang, F. L. Jiang, M. Y. Wu, C. P. Liu, K. Z. Su, W. G. Lu, D. Q. Yuan, M. C. Hong, *Nat. Commun.* **2015**, *6*, 7575.

[32] a) Y. B. He, S. C. Xiang, Z. J. Zhang, S. S. Xiong, F. R. Fronczek, R. Krishna, M. O'Keeffe, B. L. Chen, *Chem. Commun.* **2012**, *48*, 10856 – 10858; b) H. Xu, Y. B. He, Z. J. Zhang, S. C. Xiang, J. F. Cai, Y. J. Cui, Y. Yang, G. D. Qian, B. L. Chen, *J. Mater. Chem. A* **2013**, *1*, 77 – 81; c) J. P. Zhang, X. M. Chen, *J. Am. Chem. Soc.* **2009**, *131*, 5516 – 5521; d) M. Bülow, C. J. Guo, D. G. Shen, F. R. Fitch, A. I. Shirley, A. I. L. Cava, J. P. Brooks, US Patent 6024781, **2000**.

[33] P. Li, Y. B. He, Y. F. Zhao, L. H. Weng, H. L. Wang, R. Krishna, H. Wu, W. Zhou, M. O'Keeffe, Y. Han, B. L. Chen, *Angew. Chem. Int. Ed.* **2015**, *54*, 574 – 577; *Angew. Chem.* **2015**, *127*, 584 – 587.

[34] A. L. Speka, *J. Appl. Crystallogr.* **2003**, *36*, 7 – 13.

[35] A. L. Spek, *Acta Crystallogr. Sect. A* **1990**, *46*, C34.

[36] a) H. Chevreau, T. Devic, F. Salles, G. Maurin, N. Stock, C. Serre, *Angew. Chem. Int. Ed.* **2013**, *52*, 5056 – 5060; *Angew. Chem.* **2013**, *125*, 5160 – 5164; b) L. Valenzano, B. Civalleri, S. Chavan, *Chem. Mater.* **2011**, *23*, 1700 – 1718.

[37] A. Schaate, P. Roy, A. Godt, J. Lippke, F. Waltz, M. Wiebcke, P. Behrens, *Chem. Eur. J.* **2011**, *17*, 6643 – 6651.

[38] V. Colombo, S. Galli, H. J. Choi, G. D. Han, A. Maspero, G. Palmisano, N. Masciocchic, J. R. Long, *Chem. Sci.* **2011**, *2*, 1311 – 1319.

[39] C. Yang, U. Kaipa, Q. Z. Mather, X. P. Wang, V. Nesterov, A. F. Venero, M. A. Omary, *J. Am. Chem. Soc.* **2011**, *133*, 18094 – 18097.

[40] R. Krishna, *RSC Adv.* **2015**, *5*, 52269 – 52295.

[41] P. Giannozzi, S. Baroni, N. Bonini, M. Calandra, R. Car, C. Cavazzoni, D. Ceresoli, G. L. Chiarotti, M. Cococcioni, I. Dabo, A. Dal Corso, S. Fabris, G. Fratesi, S. de Gironcoli, R. Gebauer, U. Gerstmann, C. Gougoussis, A. Kokalj, M. Lazzeri, L. Martin-Samos, N. Marzari, F. Mauri, R. Mazzarello, S. Paolini, A. Pasquarello, L. Paulatto, C. Sbraccia, S. Scandolo, G. Sclauzero, A. P. Seitsonen, A. Smogunov, P. Umari, R. M. Wentzcovitch, *J. Phys. Condens. Matter* **2009**, *21*, 395502.

[42] T. Panda, T. Kundu, R. Banerjee, *Chem. Commun.* **2012**, *48*, 5464 – 5466.

[43] L. Wen, W. Shi, X. T. Chen, H. H. Li, P. Cheng, *Eur. J. Inorg. Chem.* **2012**, *22*, 3562 – 3568.

[44] a) G. M. Sheldrick, *Acta Crystallogr. Sect. A* **2008**, *64*, 112 – 122; b) A. V. Dolomanov, L. J. Bourhis, R. J. Gildea, J. A. K. Howard, H. Puschmann, *J. Appl. Crystallogr.* **2009**, *42*, 339 – 341.

[45] V. Barone, M. Casarin, D. Forrer, M. Pavone, M. Sambi, A. J. Vittadini, *Comput. Chem.* **2009**, *30*, 934 – 939.

[46] D. Frenkel, B. Smit, *Computational Science Series*, Academic Press, San Diego, **2002**.

[47] A. K. Rappe, C. J. Casewit, K. S. Colwell, W. A. Goddard III, W. M. Skid, *J. Am. Chem. Soc.* **1992**, *114*, 10024 – 10035.

Received: December 21, 2015
Published online on March 2, 2016

CHEMISTRY
A European Journal

Supporting Information

Extraordinary Separation of Acetylene-Containing Mixtures with Microporous Metal–Organic Frameworks with Open O Donor Sites and Tunable Robustness through Control of the Helical Chain Secondary Building Units

Zizhu Yao,[a] Zhangjing Zhang,[a] Lizhen Liu,[a] Ziyin Li,[a] Wei Zhou,[b] Yunfeng Zhao,[c, f] Yu Han,[c] Banglin Chen,[d] Rajamani Krishna,*[e] and Shengchang Xiang*[a]

chem_201505107_sm_miscellaneous_information.pdf

Contents

Figure S1. Pore size of **FJU-21a** (a) and **FJU-22a** (b)……..…….....S3

Figure S2. PXRD patterns of **FJU-21** and **FJU-22**……..…S4

Figure S3. Adsorption isotherms of C_2H_2, CO_2 and C_2H_4 on **FJU-21a** (a) and **FJU-22a** (b) at 273 K…….……...…….....S5

Figure S4. Transient breakthrough simulations for separation of equimolar C_2H_2/CO_2 mixture using **FJU-21a** at 296 K, with partial pressures of 50 kPa each……. S6

Figure S5. Probability distribution of the C_2H_2 (left) and CO_2 (right) center of mass in **FJU-22** framework, obtained from GCMC simulation……....S7

Figure S6 The interactions between C_2H_2 and **UTSA-100a**……...……S8

Figure S7. The illustration of column breakthrough for C_2H_2/CO_2 mixtures.....S9

Figure S8. Adsorption isotherms of C_2H_6, CH_4 and N_2 on **FJU-21a** and **FJU-22a**……..S10

Figure S9. Comparison of absolute component loadings for C_2H_2, C_2H_4, C_2H_6, CH_4, CO_2, and N_2 at (a) 273 K, and (b) 296 K in **FJU-21a** with the isotherm fits……S11

Figure S10. Comparison of absolute component loadings for C_2H_2, C_2H_4, C_2H_6, CH_4, CO_2, and N_2 at (a) 273 K, and (b) 296 K in **FJU-22a** with the isotherm fits…...……S12

Figure S11. Heats of adsorption of gases on **FJU-21a (a)** and **FJU-22a (b)**…….…. S13

Figure S12. The TGA of **FJU-21** (up) and **FJU-22** (bottom)……....……S14

Table S1. Crystal data and structure refinement for **FJU-21** and **FJU-22**.....S15

Table S2. Selected Bond Lengths (Å) and Bond Angles (°) for **FJU-21**.....S16

Table S3. Selected Bond Lengths (Å) and Bond Angles (°) for **FJU-22**.....S17

Table S4. Adsorption data for some representative MOFs at 296K……...S18

Table S5. *T*-dependent Dual-Langmuir parameter fits for C_2H_2, C_2H_4, C_2H_6, and CO_2 in **FJU-21**..... S19

Table S6. *T*-dependent Langmuir parameter fits for CH_4 and N_2 in **FJU-21**..... S20

Table S7. *T*-dependent Dual-Langmuir parameter fits for C_2H_2, C_2H_4, C_2H_6, and CO_2 in

FJU-22.....S21

Table S8. *T*-dependent Langmuir parameter fits for CH_4 and N_2 in **FJU-22**.....S22

Table S9. Data for the adsorption of C_2H_2 in **FJU-21a** at 273K.....S23

Table S10. Data for the adsorption of C_2H_4 in **FJU-21a** at 273K.....S24

Table S11. Data for the adsorption of CO_2 in **FJU-21a** at 273K.....S25

Table S12. Data for the adsorption of C_2H_2 in **FJU-21a** at 296K.....S26

Table S13. Data for the adsorption of C_2H_4 in **FJU-21a** at 296K.....S27

Table S14. Data for the adsorption of CO_2 in **FJU-21a** at 296K.....S28

Table S15. Data for the adsorption of C_2H_2 in **FJU-22a** at 273K.....S29

Table S16. Data for the adsorption of C_2H_4 in **FJU-22a** at 273K.....S30

Table S17. Data for the adsorption of CO_2 in **FJU-22a** at 273K.....S31

Table S18. Data for the adsorption of C_2H_2 in **FJU-22a** at 296K.....S32

Table S19. Data for the adsorption of C_2H_4 in **FJU-22a** at 296K.....S33

Table S20. Data for the adsorption of CO_2 in **FJU-22a** at 296K.....S34

References.....S35

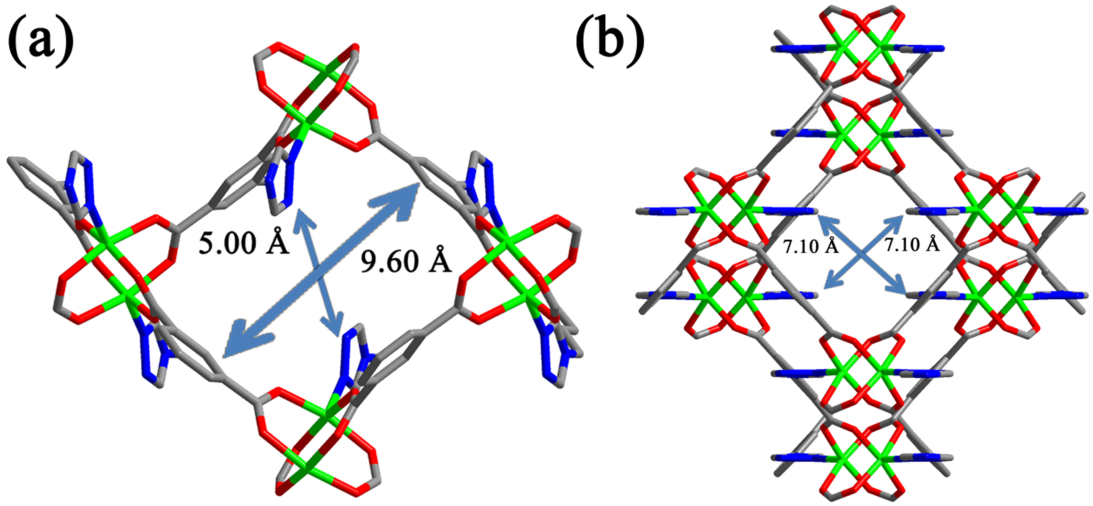

Figure S1. Pore size of **FJU-21a** (a) and **FJU-22a** (b).

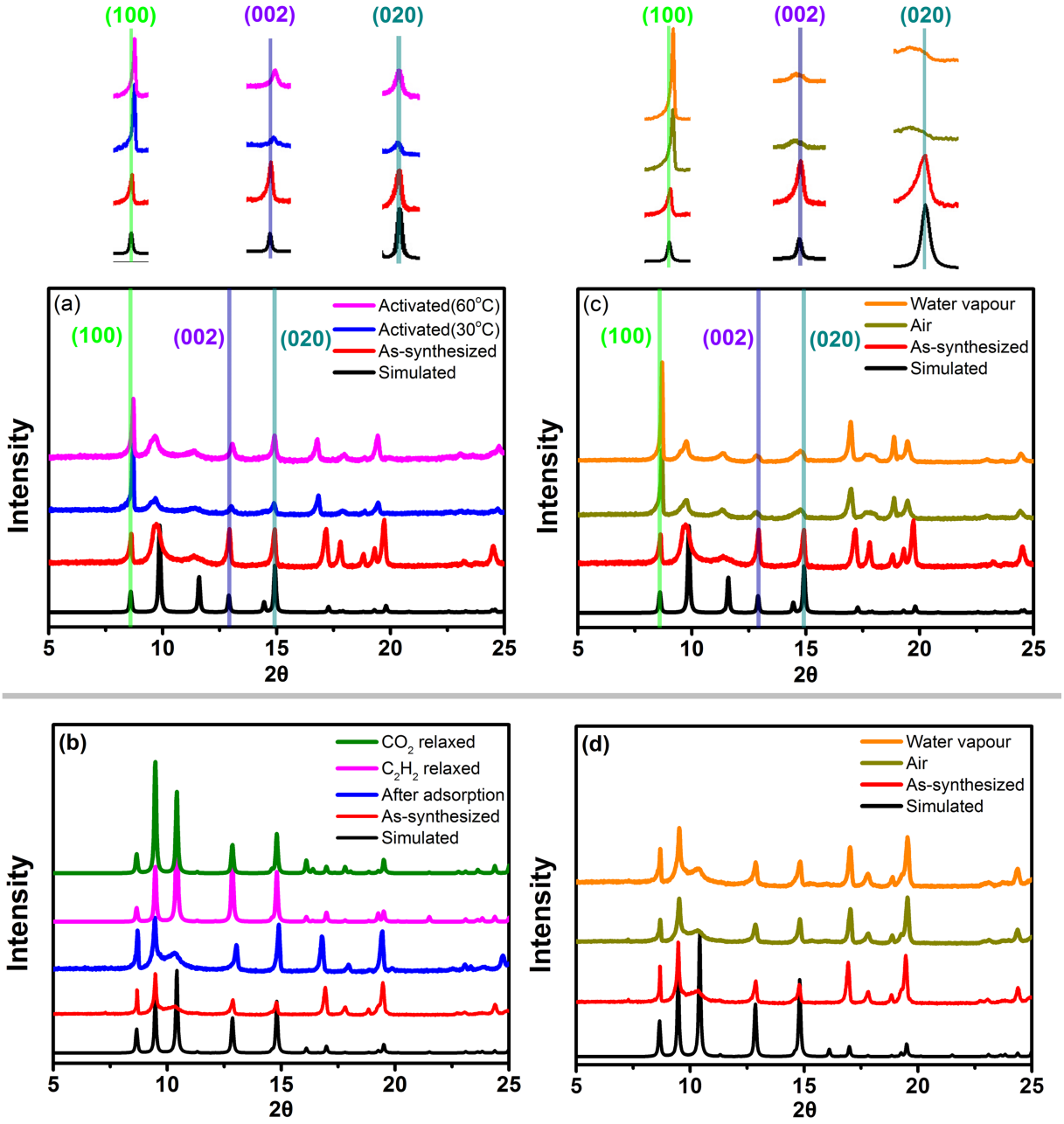

Figure S2. a & c) PXRD patterns of **FJU-21** from simulated or in various conditions. The top presents the enlarged parts oriented at (100), (002) and (020) planes; b & d) PXRD pattern of **FJU-22** from simulated or in various conditions. The test samples were exposed to air over 3 months or to water vapor for 12 hours.

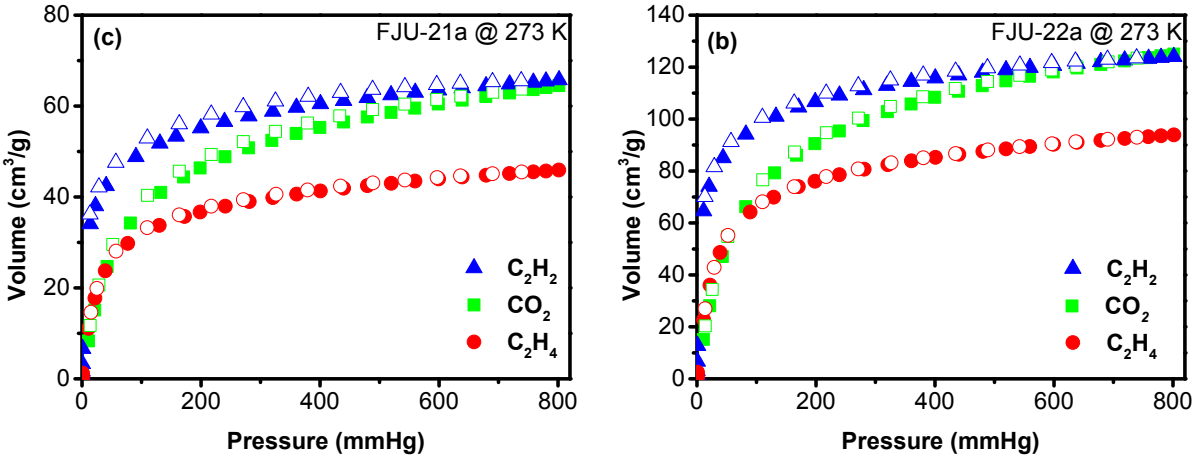

Figure S3. Adsorption isotherms of C_2H_2, CO_2 and C_2H_4 on **FJU-21a** (a) and **FJU-22a** (b) at 273 K (solid symbols: adsorption; open symbols: desorption)

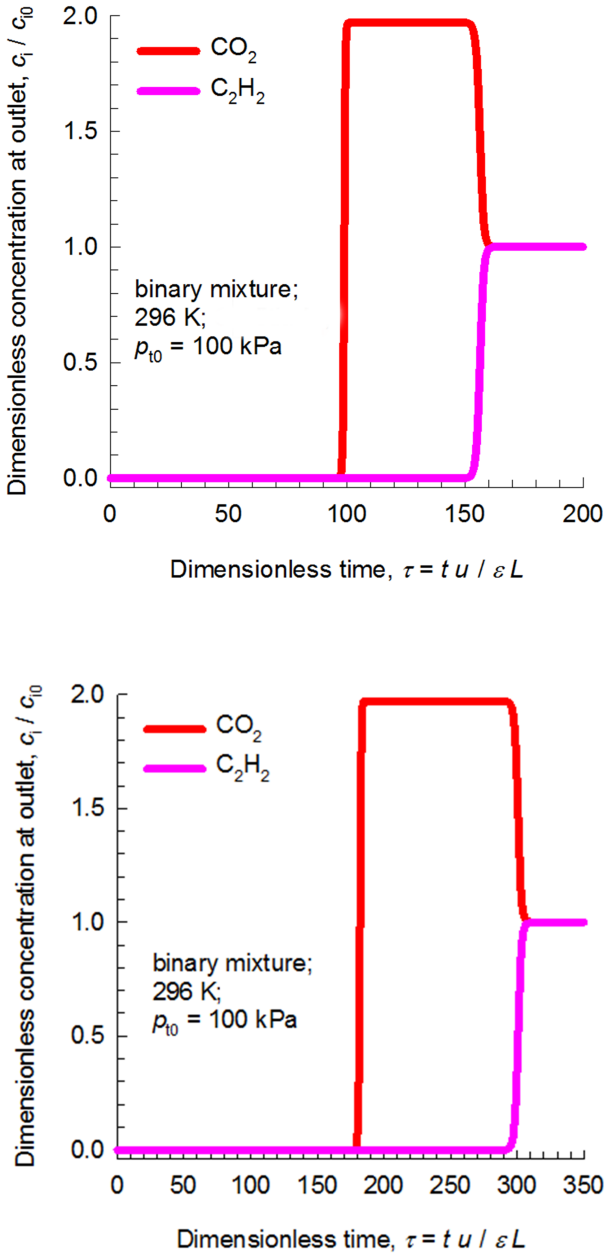

Figure S4. Transient breakthrough simulations for separation of equimolar C_2H_2/CO_2 mixture using **FJU-21a** (up) and **FJU-22a** (bottom) at 296 K, with partial pressures of 50 kPa each.

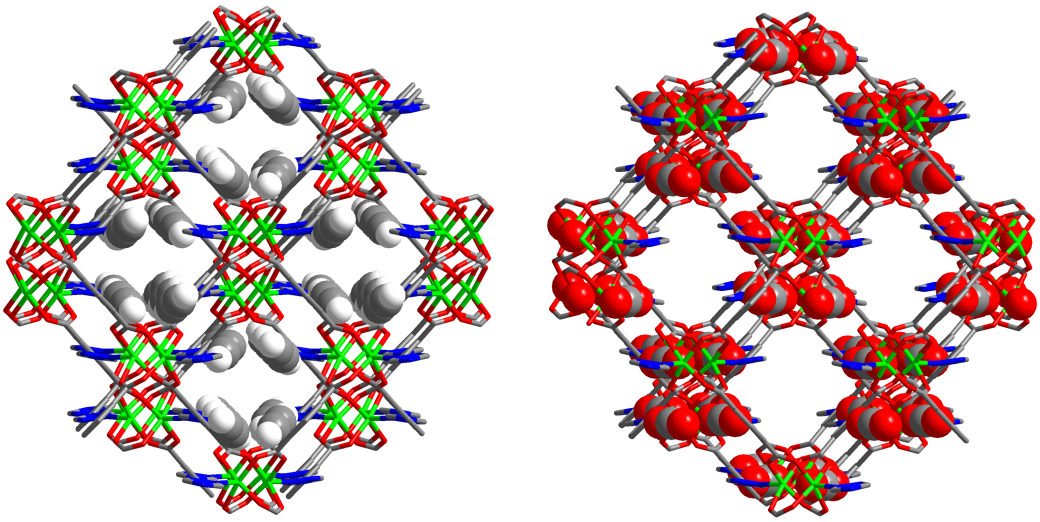

Figure S5. Probability distribution of the C_2H_2 (left) and CO_2 (right) center of mass in **FJU-22** framework, obtained from GCMC simulation at 296 K, and 1 bar.

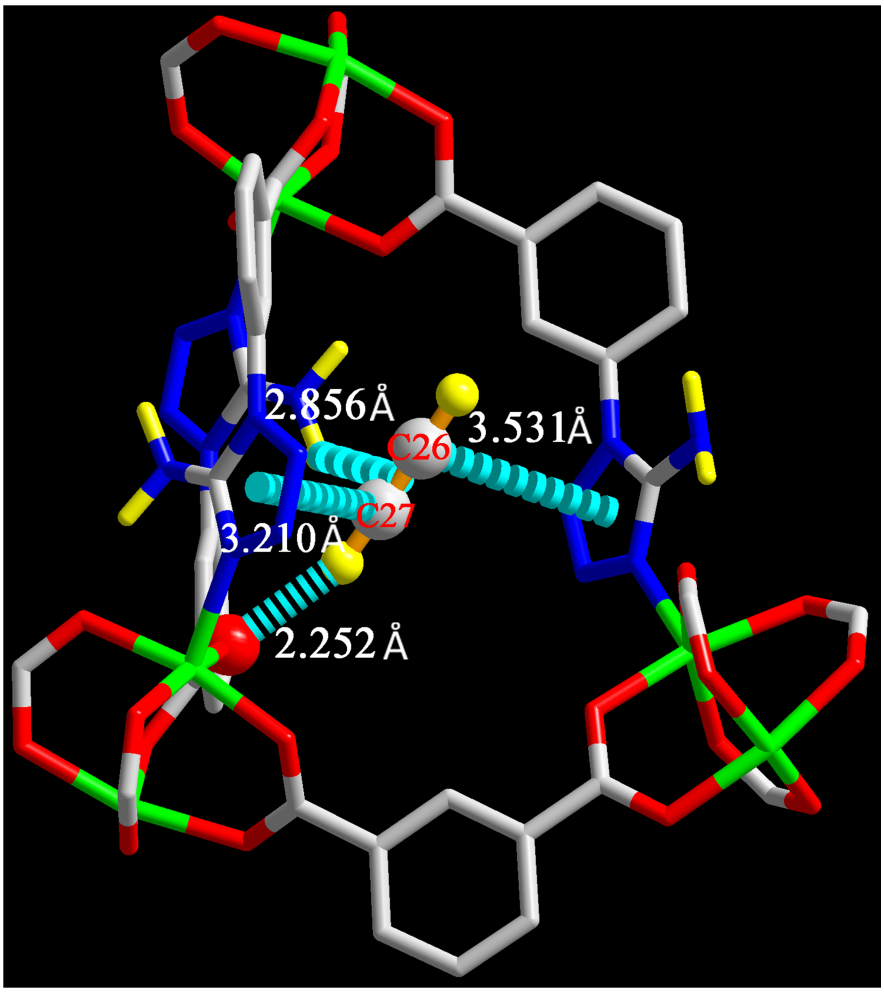

Figure S6. The interactions between C_2H_2 and **UTSA-100a.** (Multiple-point interactions of the C_2H_2 with framework: d [O (-CO_2) ··· H (C_2H_2)] = 2.252 Å, d [H (-NH2) ··· (C2H2)] = 2.856Å), d [Center (tetrazole rings) ··· C26 (C_2H_2)] = 3.531 Å, d [Center (tetrazole rings) ··· C27 (C_2H_2)] = 3.210 Å. Color code: Cu, green; C, gray; H, yellow; O, red; N, blue.

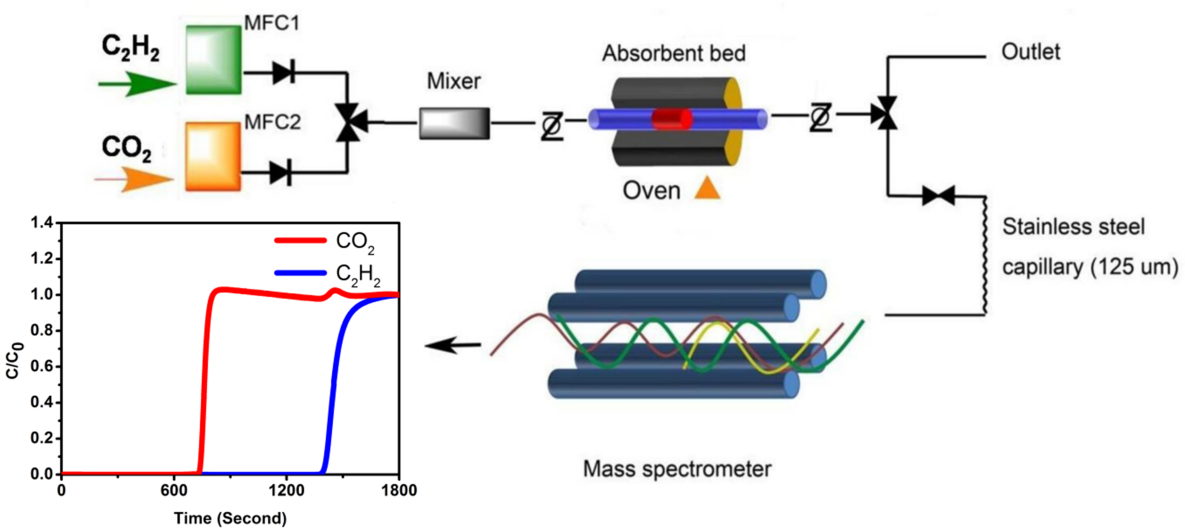

Figure S7. The illustration of Column breakthrough for C_2H_2/CO_2 mixtures.

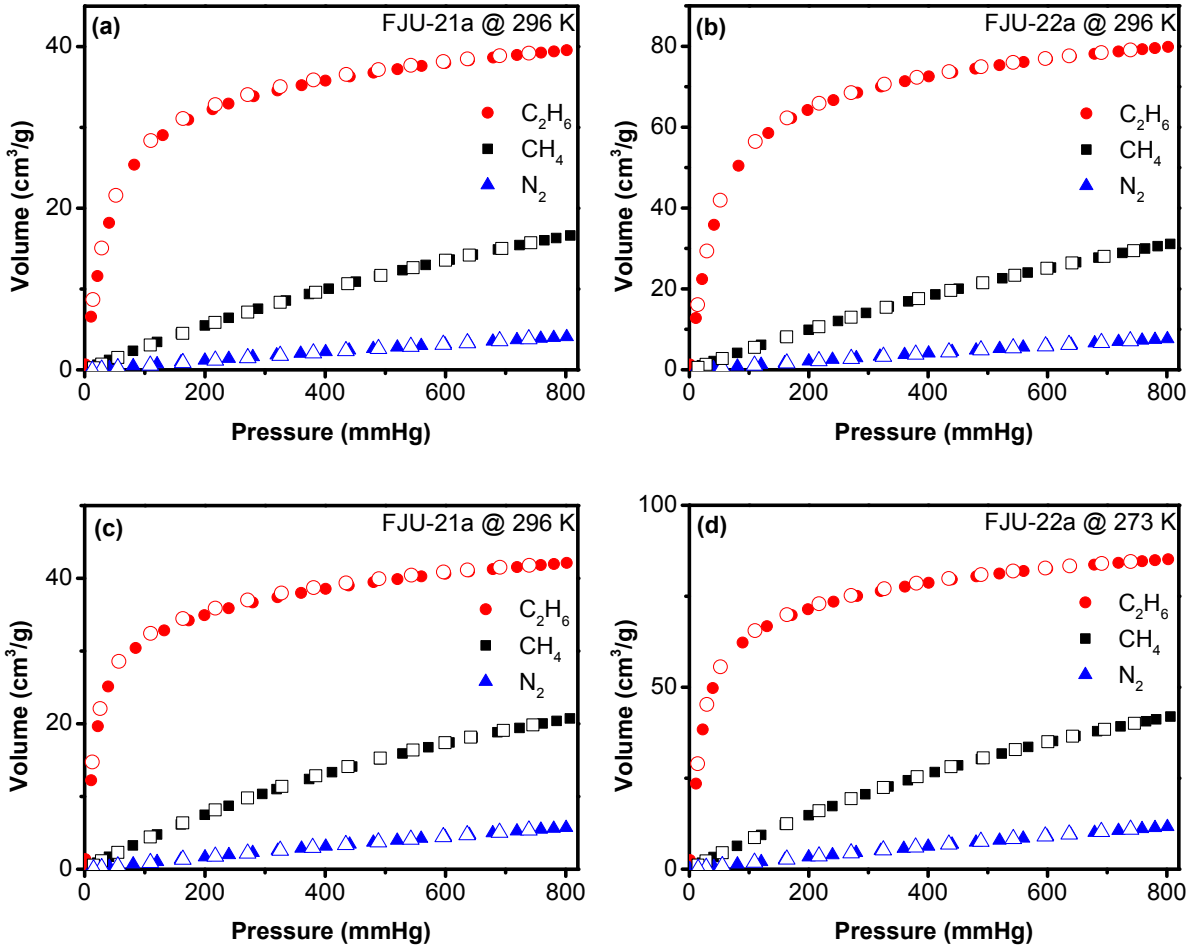

Figure S8. Adsorption isotherms of C_2H_6, CH_4 and N_2 on **FJU-21a** at (a) 296 K and (c) 273 K and **FJU-22a** at (b) 296 K and (d) 273 K (solid symbols: adsorption; open symbols: desorption)

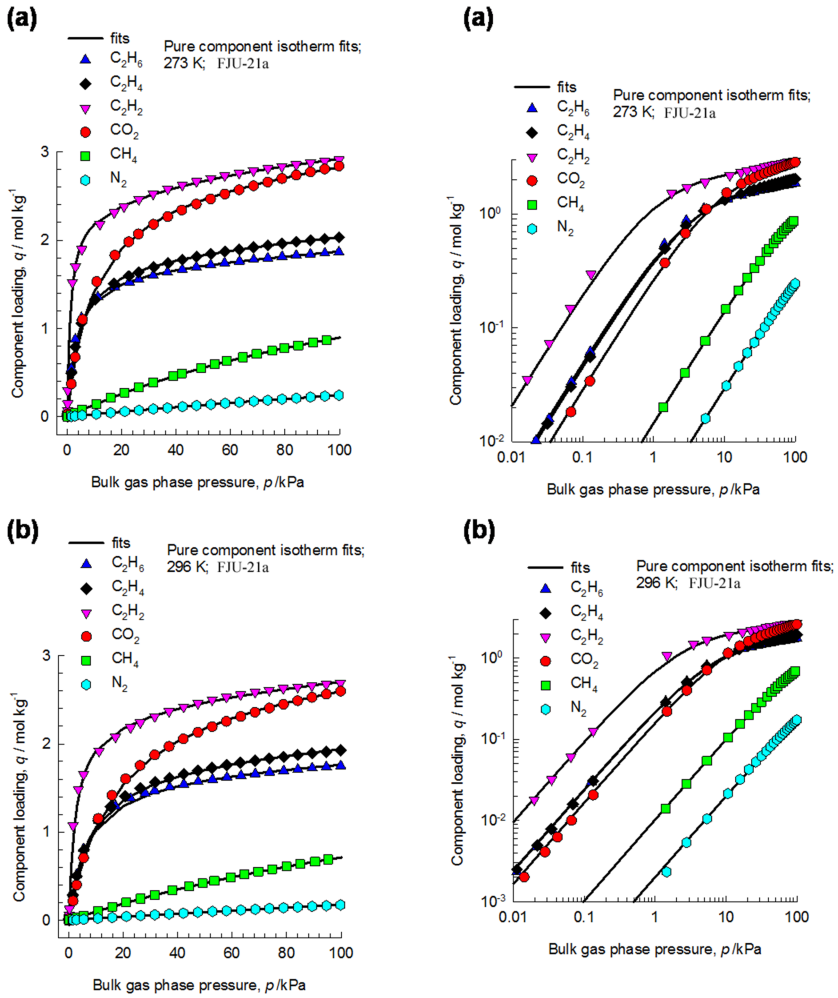

Figure S9. Comparison of absolute component loadings for C_2H_2, C_2H_4, C_2H_6, CH_4, CO_2, and N_2 at (a) 273 K, and (b) 296 K in **FJU-21a** with the isotherm fits. The plots are presented both with linear axes or logarithmic axes.

The experimentally measured excess loadings for C_2H_2, C_2H_4, C_2H_6, and CO_2 in **FJU-21a** and **FJU-22a** at temperatures of 273 K, and 296 K in **FJU-21a** and **FJU-22a** were fitted with the Dual-site Langmuir model

$$q = q_{A,sat}\frac{b_A p}{1+b_A p} + q_{B,sat}\frac{b_B p}{1+b_B p} \qquad (1)$$

with T-dependent parameters

$$b_A = b_{A0}\exp\left(\frac{E_A}{RT}\right); \quad b_B = b_{B0}\exp\left(\frac{E_B}{RT}\right) \qquad (2)$$

The parameters are provided in Table S5 and S7.

The isotherm data for CH_4, and N_2 in **FJU-21a** and **FJU-22a** were fitted with the single-site Langmuir model

$$q = q_{A,sat}\frac{b_A p}{1+b_A p} \qquad (3)$$

with T-dependent parameter

$$b_A = b_{A0}\exp\left(\frac{E_A}{RT}\right) \qquad (4)$$

The parameters are provided in Table S6 and S8.

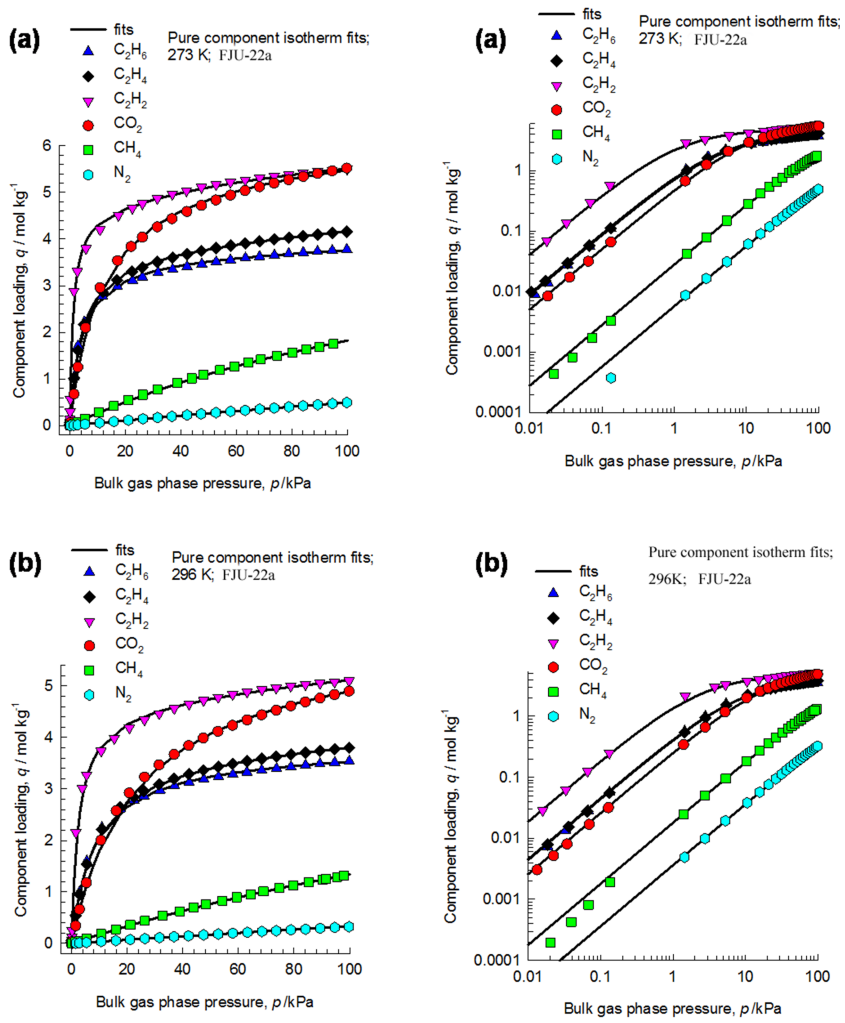

Figure S10. Comparison of absolute component loadings for C_2H_2, C_2H_4, C_2H_6, CH_4, CO_2, and N_2 at (a) 273 K, and (b) 296 K in **FJU-22a** with the isotherm fits. The plots are presented both with linear axes or logarithmic axes.

As illustration of the goodness of the fits, Figure S9 and Figure S10 present a comparison of absolute component loadings for C_2H_2, C_2H_4, C_2H_6, CH_4, CO_2, and N_2 at 273 K, and 296 K in **FJU-21** and **FJU-22** with the isotherm fits. The fits are good for all components over the entire pressure range.

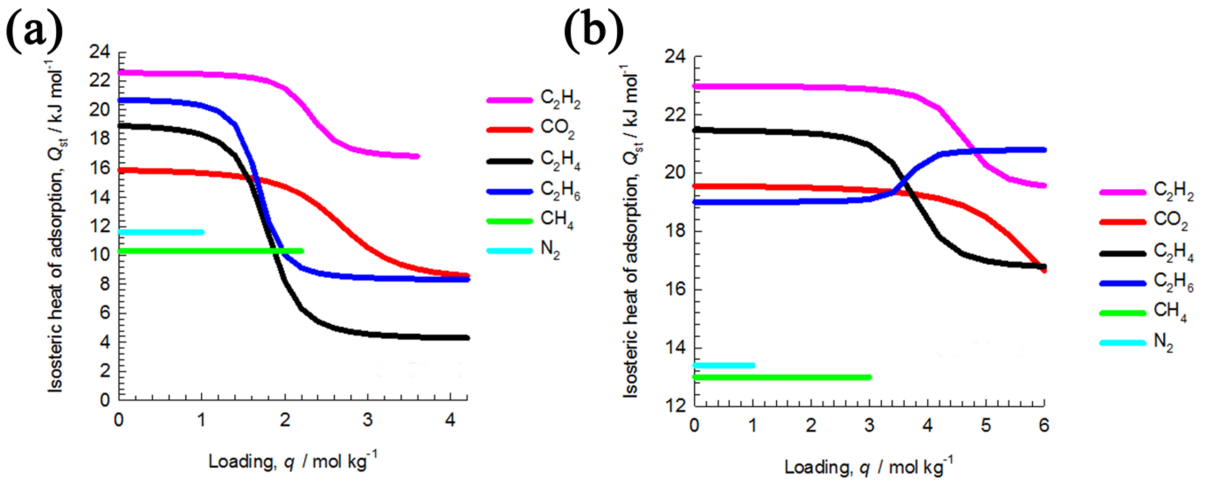

Figure S11. Heats of adsorption of gases on **FJU-21a (a)** and **FJU-22a (b)**.

The binding energies of C_2H_2, C_2H_4, C_2H_6, CH_4, CO_2, and N_2 in **FJU-21** and **FJU-22** are reflected in the isosteric heat of adsorption, Q_{st}, defined as

$$Q_{st} = RT^2 \left(\frac{\partial \ln p}{\partial T} \right)_q \qquad (5)$$

These values were determined using the pure component isotherm fits. Figure S11 present data on the loading dependence of Q_{st} for C_2H_2, C_2H_4, C_2H_6, CH_4, CO_2, and N_2 in **FJU-21a** and **FJU-22a**. At loadings below 3 mol/kg, the values of Q_{st} of **FJU-21a** and **FJU-22a** follow the hierarchy $C_2H_2 > C_2H_4 > CO_2 > C_2H_6 > N_2 \approx CH_4$.

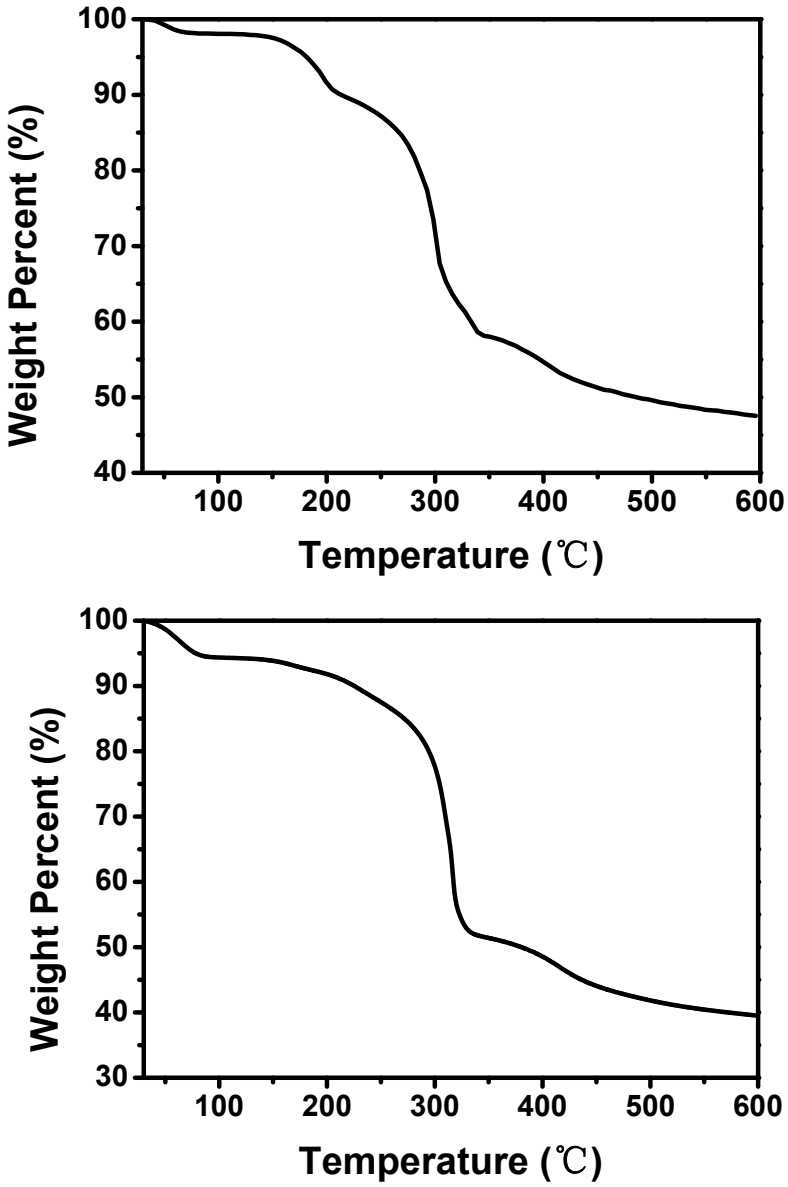

Figure S12. The TGA of **FJU-21** (up) and **FJU-22** (bottom).

Table S1. Crystal data and structure refinement for FJU-21 and FJU-22.

Identification code	**FJU-21**	**FJU-22**
Empirical formula	$Cu(C_{10}H_5O_4N_3)$	$Cu(C_{10}H_5O_4N_3)$
Formula weight	294.71	294.71
Temperature/K	291.87(13)	291.74(13)
Crystal system	monoclinic	orthorhombic
Space group	$P2_1/c$	$Pbcn$
a/Å	10.9121(3)	12.1311(5)
b/Å	11.8420(3)	14.5924(7)
c/Å	14.5557(5)	20.4168(10)
α/°	90	90
β/°	109.471(3)	90
γ/°	90	90
Volume/Å^3	1773.35(10)	3614.2(3)
Z	4	8
ρ_{calc}g/cm^3	1.104	1.083
μ/mm^{-1}	1.829	1.795
F(000)	588.0	1176.0
Crystal size/mm^3	0.01 × 0.02 × 0.1	0.1 × 0.1 × 0.12
Radiation	Cu $K\alpha$ (λ = 1.54184)	Cu $K\alpha$ (λ = 1.54184)
2θ range for data collection/°	8.594 to 134.09	8.662 to 134.122
Index ranges	$-13 \le h \le 13$, $-14 \le k \le 10$, $-17 \le l \le 18$	$-14 \le h \le 10$, $-17 \le k \le 12$, $-25 \le l \le 23$
Reflections collected	10630	11549
Independent reflections	3153 [R_{int} = 0.0480, R_{sigma} = 0.0482]	3225 [R_{int} = 0.0686, R_{sigma} = 0.0675]
Data/restraints/parameters	3153/0/163	3225/0/163
Goodness-of-fit on F^2	1.048	0.949
Final R indexes [I>=2σ (I)]	R_1 = 0.0472, wR_2 = 0.1313	R_1= 0.0570, wR_2= 0.1529
Final R indexes [all data]	R_1= 0.0576, wR_2= 0.1381	R_1= 0.0732, wR_2= 0.1633
Largest diff. peak/hole / Å^{-3}	0.95/-0.49	0.97/-0.69

Table S2. Selected Bond Lengths (Å) and Bond Angles (°) for FJU-21.

Bond	Dist	Bond	Dist
Cu(1)-O(1)	1.971(2)	Cu(1)-O(3)#3	1.969(2)
Cu(1)-O(4)#2	1.969(2)	Cu(1)-N(2)	2.160(2)
Cu(1)-O(2) #1	1.967(2)		
Angle	(°)	Angle	(°)
O(1)-Cu(1)-N(2)	92.24(11)	O(2)#1-Cu(1)-O(1)	166.38(11)
O(4)#2-Cu(1)-O(1)	86.91(12)	O(2)#1-Cu(1)-O(4)#2	89.49(12)
O(4)#2-Cu(1)-O(3)#3	166.64(10)	O(2)#1-Cu(1)-O(3)#3	90.52(11)
O(4)#2-Cu(1)-N(2)	91.57(10)	O(2)#1-Cu(1)-N(2)	100.99(10)
O(3)#3-Cu(1)-N(2)	101.53(10)	O(3)#3-Cu(1)-O(1)	89.97(11)

Symmetry transformations used to generate equivalent atoms:

#1 -X,1-Y,-Z; #2 1-X,1-Y,-Z; #3 -1+X,+Y,+Z;

#4 1+X,+Y,+Z; #5 1-X,1/2+Y,1/2-Z; #6 1-X,-1/2+Y,1/2-Z

Table S3. Selected Bond Lengths (Å) and Bond Angles (°) for FJU-22.

Bond	Dist	Bond	Dist
Cu(1)-O(1)#1	1.969(3)	Cu(1)-O(4)	1.967(3)
Cu(1)-O(3)#1	1.985(3)	Cu(1)-N(1)	2.150(3)
Cu(1)-O(2)	1.979(3)		
Angle	(°)	Angle	(°)
O(1)#1-Cu(1)-O(3)#1	166.00(12)	O(4)-Cu(1)-O(2)	167.34(11)
O(1)#1-Cu(1)-O(2)	90.17(13)	O(4)-Cu(1)-N(1)	92.88(12)
O(1)#1-Cu(1)-N(1)	95.13(12)	O(3)#1-Cu(1)-N(1)	98.45(12)
O(4)-Cu(1)-O(1)#1	86.64(13)	O(2)-Cu(1)-O(3)#1	90.93(13)
O(4)-Cu(1)-O(3)#1	89.26(13)	O(2)-Cu(1)-N(1)	99.61(12)

Symmetry transformations used to generate equivalent atoms:

#1 -X,+Y,1/2-Z; #2 1/2-X,1/2-Y,1/2+Z; #3 1-X,1-Y,-Z; #4 1/2-X,1/2-Y, -1/2+Z

Table S4. Adsorption data for some representative MOFs at 296K.[1-4]

	M'MOF-3a	**MgMOF-74**	**CoMOF-74**	**FeMOF-74**	**NOTT-300**	**UTSA-100a**	**FJU-22**
Functional groups	framework flexibility	open metal sites	open metal sites	open metal sites	phenyl rings, aromatic C–H groups, O-H groups	amino groups, tetrazole ring, metal center O	open O donors, triazole rings
Surface area (m^2/g; BET)	110	927	1018	1350	1370	970	828
Selectivity for C_2H_2/C_2H_4	24.0[a]	2.2[a]	1.7[a]	2.1[a]	2.2[a]	(10.7)[a]/(13.8)[b]	25.8[b]
Static C_2H_2 uptake at 1.0 bar (mmol/g)	1.90	8.37	8.17	6.80[c]	6.34[d]	4.27	5.12
Static C_2H_4 uptake at 1.0 bar (mmol/g)	0.40	7.45	7.02	6.10[c]	4.28[d]	1.66	3.83
Q_{st} (C_2H_2, kJ/mol)[e]	25	41	45	46	32	22	23

a IAST analysis for ethylene/acetylene mixtures containing 1% acetylene at 100 kPa.

b Selectivity for ethylene/acetylene mixtures containing 1% acetylene at 100 kPa calculated from breakthrough experiment.

c At 318 K.

d At 293 K.

e Q_{st} values are the enthalpy at zero coverage.

Table S5. *T*- dependent Dual-Langmuir parameter fits for C_2H_2, C_2H_4, C_2H_6, and CO_2 in FJU-21.

	Site A			Site B		
	$q_{A,sat}$ mol kg^{-1}	b_{A0} Pa^{-1}	E_A kJ mol^{-1}	$q_{B,sat}$ mol kg^{-1}	b_{B0} Pa^{-1}	E_B kJ mol^{-1}
C_2H_2	2.3	4.29×10^{-8}	22.6	1.4	5.45×10^{-9}	16.7
C_2H_4	1.8	5.65×10^{-8}	19.1	3	1.76×10^{-7}	4.2
C_2H_6	1.7	3.07×10^{-8}	20.8	5	1.23×10^{-8}	8.3
CO_2	5.7	1.83×10^{-8}	8.2	2.7	9.17×10^{-8}	16

Table S6. *T*- dependent Langmuir parameter fits for CH_4, and N_2 in FJU-21.

	$q_{A,sat}$ mol kg^{-1}	b_{A0} Pa^{-1}	E_B kJ mol^{-1}
CH_4	2.3	6.64×10^{-8}	10.3
N_2	1.3	1.39×10^{-8}	11.6

Table S7. *T*- dependent Dual-Langmuir parameter fits for C_2H_2, C_2H_4, C_2H_6, and CO_2 in FJU-22.

	Site A			Site B		
	$q_{A,sat}$ mol kg^{-1}	b_{A0} Pa^{-1}	E_A kJ mol^{-1}	$q_{B,sat}$ mol kg^{-1}	b_{B0} Pa^{-1}	E_B kJ mol^{-1}
C_2H_2	4.6	3.57×10^{-8}	23	2.3	1.4×10^{-9}	19.4
C_2H_4	3.8	1.87×10^{-8}	21.5	6.5	5.49×10^{-10}	16.7
C_2H_6	3.7	5.49×10^{-8}	19	6	3.77×10^{-11}	20.8
CO_2	3.0	2.09×10^{-9}	14.7	5.7	1.57×10^{-8}	19.6

Table S8. *T*- dependent Langmuir parameter fits for CH_4, and N_2 in FJU-22.

	$q_{A,sat}$ mol kg^{-1}	b_{A0} Pa^{-1}	E_B kJ mol^{-1}
CH_4	5.2	1.76×10^{-8}	13
N_2	3.6	4.35×10^{-9}	13.4

Table S9. Data for the adsorption of C_2H_2 in FJU-21a at 273K

Pressure (mmHg)	Adsorption (cm^3/g)	Pressure (mmHg)	Adsorption (cm^3/g)	Pressure (mmHg)	Adsorption (cm^3/g)
0.018	0.094	320.648	58.802	635.831	64.959
0.035	0.198	360.452	59.684	596.071	64.674
0.061	0.366	400.596	60.481	542.585	64.204
0.125	0.788	439.729	61.176	488.352	63.628
0.255	1.645	479.454	61.817	434.635	62.937
0.506	3.313	519.442	62.422	380.116	62.098
0.994	6.630	559.992	62.986	325.167	61.061
13.653	34.064	599.062	63.477	270.998	59.798
22.573	38.026	638.867	63.949	217.131	58.188
40.515	42.449	679.096	64.399	163.411	56.041
90.545	48.821	718.565	64.807	109.752	52.913
130.822	51.791	758.428	65.195	56.855	47.579
158.059	53.316	779.776	65.468	28.518	42.168
199.498	55.148	801.616	65.732	13.410	36.198
239.471	56.572	738.132	65.513		
280.469	57.772	689.772	65.302		

Table S10. Data for the adsorption of C_2H_4 in FJU-21a at 273K

Pressure (mmHg)	Adsorption (cm^3/g)	Pressure (mmHg)	Adsorption (cm^3/g)	Pressure (mmHg)	Adsorption (cm^3/g)
0.053	0.078	320.678	39.864	689.839	45.117
0.104	0.147	360.712	40.633	636.095	44.654
0.147	0.202	400.696	41.326	596.764	44.279
0.241	0.324	439.758	41.930	542.607	43.728
0.516	0.680	479.610	42.493	488.881	43.103
0.968	1.247	519.685	43.017	434.327	42.395
10.965	11.108	559.629	43.512	379.111	41.545
21.744	17.748	599.420	43.969	326.215	40.604
38.974	23.763	638.962	44.399	271.243	39.426
76.827	29.805	679.141	44.796	217.258	37.980
129.812	33.743	718.425	45.158	163.432	36.073
172.290	35.710	758.537	45.521	109.716	33.268
198.568	36.688	779.825	45.719	57.261	28.086
240.778	37.976	801.375	45.926	24.991	19.892
281.086	38.993	738.896	45.500	15.094	14.645

Table S11. Data for the adsorption of CO_2 in FJU-21a at 273K

Pressure (mmHg)	Adsorption (cm^3/g)	Pressure (mmHg)	Adsorption (cm^3/g)	Pressure (mmHg)	Adsorption (cm^3/g)
0.086	0.060	359.903	53.972	636.574	62.177
0.160	0.120	399.801	55.297	596.101	61.472
0.263	0.203	439.674	56.490	542.467	60.433
0.517	0.410	479.534	57.597	488.192	59.242
0.955	0.764	519.451	58.609	433.135	57.847
10.948	8.339	559.220	59.559	379.023	56.270
21.392	15.137	598.925	60.452	325.262	54.420
42.388	24.715	638.900	61.300	271.236	52.172
81.376	34.274	678.693	62.102	217.273	49.353
132.479	41.006	718.449	62.877	163.609	45.663
170.823	44.399	758.163	63.625	110.188	40.368
198.477	46.383	779.806	64.078	51.762	29.549
240.269	48.848	801.271	64.505	28.413	20.635
280.022	50.806	739.013	63.721	13.788	11.730
319.172	52.459	690.316	63.033		

Table S12. Data for the adsorption of C_2H_2 in FJU-21a at 296K

Pressure (mmHg)	Adsorption (cm^3/g)	Pressure (mmHg)	Adsorption (cm^3/g)	Pressure (mmHg)	Adsorption (cm^3/g)
0.036	0.082	320.092	54.173	690.242	60.492
0.068	0.167	359.831	55.117	636.403	60.284
0.149	0.403	399.655	55.953	596.681	60.068
0.262	0.715	439.529	56.686	543.071	59.674
0.490	1.359	479.201	57.326	488.615	59.140
1.016	2.837	519.691	57.912	434.854	58.459
11.199	24.027	558.894	58.412	380.688	57.603
26.383	33.238	598.675	58.866	325.344	56.488
40.783	37.021	638.498	59.271	271.344	55.138
83.926	42.928	678.243	59.629	217.283	53.393
129.831	46.544	718.180	59.944	163.518	51.088
171.916	48.919	757.987	60.218	109.877	47.782
198.989	50.191	779.435	60.425	56.788	42.348
239.374	51.753	801.433	60.612	29.083	36.632
279.353	53.042	738.627	60.586	13.514	28.847

Table S13. Data for the adsorption of C_2H_4 in FJU-21a at 296K

Pressure (mmHg)	Adsorption (cm^3/g)	Pressure (mmHg)	Adsorption (cm^3/g)	Pressure (mmHg)	Adsorption (cm^3/g)
0.085	0.056	359.965	37.964	636.179	42.246
0.164	0.111	399.015	38.699	596.270	41.848
0.261	0.176	440.179	39.386	542.692	41.264
0.521	0.355	478.554	39.982	488.530	40.587
1.012	0.690	519.805	40.554	434.227	39.808
10.691	6.406	559.429	41.064	380.669	38.917
21.215	11.260	599.333	41.537	325.155	37.812
40.881	17.795	638.862	41.971	271.038	36.494
81.481	25.306	678.864	42.394	217.056	34.811
116.992	28.878	718.458	42.784	163.459	32.520
157.096	31.523	758.521	43.164	110.021	28.976
198.900	33.486	779.773	43.369	57.800	22.299
240.468	34.977	801.295	43.585	29.167	14.827
280.468	36.151	738.689	43.138	13.437	8.217
320.570	37.129	690.160	42.738		

Table S14. Data for the adsorption of CO_2 in FJU-21a at 296K

Pressure (mmHg)	Adsorption (cm^3/g)	Pressure (mmHg)	Adsorption (cm^3/g)	Pressure (mmHg)	Adsorption (cm^3/g)
0.107	0.045	359.878	47.729	636.623	56.403
0.211	0.092	399.834	49.198	596.279	55.631
0.316	0.141	439.400	50.507	542.276	54.467
0.499	0.225	479.468	51.729	488.074	53.137
1.010	0.463	519.399	52.843	434.155	51.644
11.144	4.951	559.231	53.884	379.321	49.876
21.120	8.966	598.912	54.845	325.094	47.815
40.667	15.863	638.644	55.748	271.008	45.335
81.246	25.839	678.520	56.603	217.439	42.247
119.533	31.739	718.516	57.405	163.734	38.132
157.880	35.912	758.483	58.162	110.235	32.225
198.746	39.299	779.473	58.591	51.270	20.677
239.134	41.957	801.599	59.024	26.912	12.570
279.161	44.162	739.312	58.137	15.114	7.679
319.149	46.049	690.516	57.348		

Table S15. Data for the adsorption of C_2H_2 in FJU-22a at 273K

Pressure (mmHg)	Adsorption (cm^3/g)	Pressure (mmHg)	Adsorption (cm^3/g)	Pressure (mmHg)	Adsorption (cm^3/g)
0.026	0.284	319.096	112.875	635.993	122.211
0.039	0.418	360.274	114.418	596.097	121.616
0.061	0.693	400.551	115.750	542.665	120.706
0.131	1.551	439.719	116.885	488.183	119.621
0.245	3.064	480.190	117.954	434.646	118.349
0.525	6.681	519.401	118.902	380.268	116.829
0.982	12.736	559.639	119.789	325.037	114.960
11.093	64.591	599.100	120.573	271.096	112.717
20.357	74.017	638.836	121.317	217.259	109.863
43.885	85.028	678.717	122.004	163.434	106.074
82.307	94.120	718.678	122.652	110.027	100.564
132.744	100.974	759.010	123.267	57.292	91.244
170.802	104.515	779.897	123.631	29.085	81.562
198.750	106.631	801.318	123.994	13.342	70.076
239.453	109.137	738.832	123.447		
280.192	111.202	690.049	122.915		

Table S16. Data for the adsorption of C_2H_4 in FJU-22a at 273K

Pressure (mmHg)	Adsorption (cm^3/g)	Pressure (mmHg)	Adsorption (cm^3/g)	Pressure (mmHg)	Adsorption (cm^3/g)
0.038	0.113	320.829	82.417	690.247	92.209
0.080	0.222	360.440	83.915	636.688	91.271
0.125	0.337	400.760	85.258	596.619	90.508
0.255	0.665	440.287	86.436	542.228	89.380
0.506	1.289	480.506	87.534	488.782	88.132
1.005	2.499	519.425	88.515	434.663	86.725
11.357	22.775	559.368	89.420	380.407	85.084
21.872	36.059	599.441	90.277	326.246	83.174
38.950	48.655	638.929	91.055	271.043	80.801
89.442	64.202	678.870	91.805	217.143	77.873
128.958	69.938	718.883	92.517	163.457	73.963
170.492	73.968	758.522	93.186	110.139	68.141
198.356	76.055	779.930	93.539	52.086	55.209
239.268	78.584	801.431	93.904	28.909	42.887
281.069	80.707	739.269	93.005	13.781	26.977

Table S17. Data for the adsorption of CO_2 in FJU-22a at 273K

Pressure (mmHg)	Adsorption (cm^3/g)	Pressure (mmHg)	Adsorption (cm^3/g)	Pressure (mmHg)	Adsorption (cm^3/g)
0.070	0.093	359.924	105.791	637.270	120.315
0.134	0.189	399.676	108.378	596.109	118.890
0.271	0.390	439.668	110.715	542.472	116.838
0.491	0.715	479.487	112.824	488.331	114.482
1.010	1.482	519.216	114.730	434.259	111.775
10.833	15.165	559.129	116.502	379.461	108.574
21.331	28.122	598.781	118.133	325.080	104.844
42.709	47.076	638.891	119.654	271.367	100.360
82.055	66.276	678.624	121.061	217.540	94.728
130.450	79.284	718.494	122.385	163.869	87.307
167.577	86.067	758.287	123.647	110.646	76.620
198.188	90.525	779.782	124.338	51.887	54.762
239.238	95.420	801.410	125.017	25.768	34.391
279.251	99.400	739.861	123.424	14.019	20.358
320.043	102.843	690.933	122.010		

Table S18. Data for the adsorption of C_2H_2 in FJU-22a at 296K

Pressure (mmHg)	Adsorption (cm^3/g)	Pressure (mmHg)	Adsorption (cm^3/g)	Pressure (mmHg)	Adsorption (cm^3/g)
0.026	0.117	320.945	104.124	636.440	113.510
0.049	0.242	360.624	105.728	596.361	113.007
0.073	0.376	400.273	107.095	542.955	112.171
0.120	0.638	439.808	108.297	488.766	111.116
0.252	1.378	479.541	109.386	434.663	109.816
0.504	2.798	520.106	110.345	380.572	108.225
1.004	5.595	559.143	111.177	325.105	106.188
11.227	48.294	599.019	111.936	271.129	103.742
28.702	67.556	638.927	112.596	217.122	100.607
40.538	73.226	678.734	113.191	163.421	96.472
80.647	83.713	718.526	113.716	109.886	90.622
116.205	89.188	758.198	114.191	57.372	80.938
157.388	93.745	779.819	114.487	24.980	67.666
199.004	97.240	801.387	114.754	13.316	55.211
239.147	99.943	738.888	114.435		
280.305	102.225	690.311	114.078		

Table S19. Data for the adsorption of C_2H_4 in FJU-22a at 296K

Pressure (mmHg)	Adsorption (cm^3/g)	Pressure (mmHg)	Adsorption (cm^3/g)	Pressure (mmHg)	Adsorption (cm^3/g)
0.070	0.087	360.403	75.349	636.825	83.183
0.141	0.175	400.649	76.832	596.256	82.391
0.276	0.344	439.723	78.097	542.639	81.219
0.496	0.617	478.923	79.246	488.822	79.884
1.008	1.242	519.598	80.322	434.670	78.347
11.073	12.201	559.731	81.288	380.301	76.541
21.323	21.323	599.111	82.164	325.218	74.350
41.309	34.439	639.319	82.988	271.153	71.694
82.307	49.686	678.954	83.749	217.285	68.276
132.675	59.239	718.697	84.457	163.672	63.570
169.935	63.663	758.407	85.127	110.475	56.312
197.996	66.244	779.727	85.490	51.686	40.014
239.271	69.277	801.472	85.857	29.105	27.493
279.276	71.637	739.067	84.933	13.868	15.017
320.527	73.670	690.691	84.138		

Table S20. Data for the adsorption of CO_2 in FJU-22a at 296K

Pressure (mmHg)	Adsorption (cm^3/g)	Pressure (mmHg)	Adsorption (cm^3/g)	Pressure (mmHg)	Adsorption (cm^3/g)
0.100	0.068	359.776	89.313	637.605	105.681
0.169	0.117	399.743	92.246	596.204	103.985
0.260	0.181	439.447	94.855	542.235	101.538
0.527	0.379	479.461	97.243	488.190	98.787
0.976	0.711	519.296	99.436	434.050	95.653
10.651	7.697	559.174	101.453	380.237	92.076
21.120	14.827	598.717	103.310	325.159	87.771
39.881	26.393	638.811	105.067	271.095	82.675
79.386	44.884	678.725	106.709	217.518	76.392
121.293	57.679	718.389	108.255	163.874	68.128
157.177	65.460	758.307	109.712	110.685	56.370
198.957	72.416	779.617	110.508	51.107	33.935
238.975	77.723	801.476	111.283	29.085	21.168
279.848	82.243	739.893	109.375	14.364	11.234
319.943	86.038	691.256	107.703		

REFERENCE

1 S.C. Xiang, Z.J. Zhang, C.G. Zhao, K.L. Hong, X.B. Zhao, D.R. Ding, M.H. Xia, C.D. Wu, M.C. Das, R. Gill, K.M. Tomoas, B.L. Chen, *Nat. Commun.* **2011**, *2*, 204.

2 a) E. D. Bloch, W.L. Queen, R. Krishna, J.M. Zadrozny, C.M. Brown, J.R. Long, *Science*. **2012**, *335*, 1606–1610; b) Y.B. He, R. Krishna, B.L. Chen, *Energy Environ. Sci.* **2012**, *5*, 9107-9120.

3 S.H. Yang, A.J. Ramirez-Cuesta, R. Newby, V. Garcia-Sakai, P. Manuel, S.K. Callear, S.I. Campbell, C.C. Tang, M. Schröder, *Nat. Chem.* **2015**, *7*, 121–129.

4 T.L. Hu, H.L. Wang, B. Li, R. Krishna, H. Wu, W. Zhou, Y.F. Zhao, Y. Han, X. Wang, W.D. Zhu, Z.Z. Yao, S.C. Xiang, B.L. Chen, *Nat. Commun.* **2015**, *6*, 7328